GAS HYDRATE AND FREE GAS DETECTION USING SEISMIC QUALITY FACTOR ESTIMATES FROM HIGH-RESOLUTION P-CABLE 3D SEISMIC DATA

Sunny Singhroha[1], Stefan Bünz[1], Andreia Plaza-Faverola[1], Shyam Chand[1, 2]

[1]CAGE - Centre for Arctic Gas Hydrate, Environment and Climate, Department of Geology, UiT The Arctic University of Norway, Tromsø, Norway

[2]Geological Survey of Norway (NGU), Trondheim, Norway

sunny.singhroha@uit.no

stefan.buenz@uit.no

andreia.a.faverola@uit.no

shyam.chand@ngu.no

Original paper date of submission: 20th January, 2015

Revised paper date of submission: 14th August, 2015

ABSTRACT

Seismic attenuation in gas hydrate and free gas bearing sediments is estimated from high-resolution P-Cable 3D seismic data from Vestnesa Ridge on the Arctic continental margin of Svalbard. P-Cable data have broad bandwidth (20-300 Hz) which is extremely advantageous in estimating seismic attenuation in a medium. The seismic quality factor (Q), inverse of seismic attenuation, is estimated from the seismic dataset using centroid frequency shift method and spectral ratio method. Centroid frequency shift method establishes a relationship between the change in the centroid frequency of an amplitude spectrum and the Q value of a medium. Spectral ratio method estimates the Q value of a medium by studying the differential decay of different frequencies. Broad bandwidth and short offset characteristics of the P-Cable dataset are useful to continuously map Q for different layers throughout the 3D seismic volume. The centroid frequency shift method is found to be relatively more stable than spectral ratio method. Q values estimated using these two methods are in concordance with each other. The Q data documents attenuation anomalies in the layers in the gas hydrate stability zone above the BSR and in the free gas zone below. Changes in the attenuation anomalies correlate with small-scale fault systems in the Vestnesa Ridge suggesting a strong structural control on the distribution of free gas and gas hydrates in the region. We argue that high and spatially limited Q anomalies in the layer above the BSR indicate the presence of gas hydrates in marine sediments in this setting. Hence, the presented workflow to analyze Q using high-resolution P-cable 3D seismic data with a large bandwidth can be a potential technique to detect and directly map the distribution of gas hydrates in marine sediments.

INTRODUCTION

Gas hydrates are crystalline ice like structures normally formed at certain temperature and pressure conditions (Brooks et al., 1986). The temperature and pressure conditions required for gas hydrates formation are available in continental slope and permafrost environments (Sloan, 1998). The presence of marine gas hydrates in continental margins has been confirmed from different drilling activities (Collett and Ladd, 2000; Collett et al., 1999; Riedel et al., 2010; Ryu et al., 2013; Liu et al., 2012; Zhang et al., 2007). Seismic methods are commonly used to remotely identify gas hydrates in the marine sediments. The presence of gas hydrates in the sediments is often indicated in seismic data by a bottom simulating reflection (BSR) (Shipley et al., 1979). It marks a sharp impedance contrast between hydrate-bearing and gas-charged sediments. The BSR occurs at the base of the hydrate stability zone, which is governed mostly by pressure and temperature conditions (Sloan, 1998). Due to this control, the BSR often mimics the seafloor; therefore, cross-cuts the sedimentary strata (Shipley at al., 1979). Since the presence of gas hydrates increases the velocities, concentration of gas hydrates in sediments is usually estimated using seismic velocity models (Lee and Collett, 2001; Gei and Carcione, 2003; Ecker et al., 1998; Chand et al., 2004). The presence of gas hydrates in sediments has a pronounced effect on amplitude and frequency characteristics of a seismic signal also (Guerin and Goldberg, 2002; Pratt et al., 2003; Chand and Minshull, 2004). Hydrates in sediments show contradicting amplitude characteristics in seismic sections like amplitude blanking (Korenaga et al., 1997) and amplitude enhancements (Nouzé et al., 2004; Yoo et al., 2013, Riedel et al., 2010) at different geological settings.

Seismic signal attenuates mainly due to extrinsic attenuation (due to factors like spherical divergence, obliquity factor, scattering etc.) and intrinsic attenuation (due to conversion of vibration energy into heat energy) (Mavko et al., 1998). At seismic

frequencies, analysis on attenuation normally refers to intrinsic attenuation (Mavko et al., 1998) which can be studied through spectral analysis (Jacobson et al., 1981). Since gas hydrate increases the stiffness of the matrix (Jung et al., 2012) and P-wave velocity, it was normally assumed that the sediments saturated with gas hydrates will show lower attenuation (Wood et al., 2000). Unlike P-wave velocity, no unique trend of seismic attenuation in gas hydrates can be observed from the literature; thus making attenuation characteristic of the gas hydrate bearing sediments a debatable topic (Guerin et al., 1999; Wood et al., 2000; Chand et al., 2004; Rossi et al., 2007; Sain et al., 2009; Sain and Singh, 2011; Jaiswal et al., 2012; Dewangan et al., 2014). Laboratory experiments in hydrate bearing sediments indicated increase of attenuation with hydrate saturation (Priest et al., 2006; Best et al., 2013) whereas attenuation estimates from field experiments on gas hydrates indicated contradicting results. For example, studies on well log data (Guerin and Goldberg, 2002; Guerin and Goldberg, 2005; Matsushima, 2005), VSP data (Pratt et al., 2005; Bellefleur et al., 2007) and on cross-hole seismic data (Pratt et al., 2003; Bauer et al., 2005) indicated an increase in attenuation. Other studies, mainly on surface seismic data (Dewangan et al., 2014; Rossi et al., 2007; Matsushima, 2006) indicated a decrease in attenuation. The increase (Guerin and Goldberg, 2002; Gei and Carcione, 2003; Chand and Minshull, 2004; Lee and Collet, 2006) and decrease (Dewangan et al., 2014; Sain and Singh, 2011) in attenuation has been explained by using different rock physics models depending on the assumed micro structure of the hydrate and also sediment-hydrate mixtures. Chand and Minshull (2004) suggested that the amount of attenuation not only changes with hydrate saturation but also with the frequency of seismic signal.

The seismic quality factor (Q), inverse of seismic attenuation, can be estimated from the seismic dataset using different methods which includes the amplitude decay method (Badri and Mooney, 1987), the rise time method (Gladwin and Stacey, 1974), the centroid

92 frequency shift method (Quan and Harris, 1997), wavelet modeling (Jannsen et al., 1985), the
93 pulse broadening method (Hatherly, 1986), the spectral ratio method (Jannsen et al., 1985;
94 Båth, 1982) and the inversion method (Amundsen and Mittet, 1994). Tonn (1991) compared
95 10 methods of attenuation estimation using VSP seismograms and concluded that no single
96 method is suitable for all situations.

97 In the present study, we apply two different methods to investigate seismic
98 attenuation in gas hydrate and free gas saturated sediments from Vestnesa Ridge, a deep-
99 water gas hydrate system located offshore west-Svalbard (Figure 1). The quality factor (Q)
100 has been estimated from P-Cable seismic data using the spectral ratio method (Jannsen et al.,
101 1985) and the centroid frequency shift method (Quan and Harris, 1997). The centroid
102 frequency shift method establishes a relationship between the change in the centroid
103 frequency of an amplitude spectrum and the Q value of a medium (Quan and Harris, 1997).
104 On the contrary, the spectral ratio method estimates the Q value of a medium by studying the
105 differential decay of different frequencies (Båth, 1982). Due to limitation of seismic
106 bandwidth in conventional seismic data, it is almost impossible to map Q with high accuracy.
107 Low signal to noise ratio, short bandwidth, source/receiver array directivity and distinct
108 raypaths in a CDP gather are the main problems encountered in Q analysis from conventional
109 surface seismic data (Hustedt and Clark, 1999). But P-Cable surface seismic data is
110 essentially zero-offset (offset varying from 97-143 m) in deep water and has broad bandwidth
111 (20-300 Hz). Raypaths of different traces in a CDP gather of P-Cable data are approximately
112 similar at deep water depth as offset is quite small. Stacked P-Cable data has high signal to
113 noise ratio and the stacking process involves traces with almost similar raypaths. These
114 characteristics of P-cable data match well with the characteristics of VSP data (Galperin,
115 1985) and make P-Cable data suitable for subsurface Q analysis. Moreover, using P-Cable
116 3D seismic data for estimating Q allows us to analyze the spatial distribution of Q which can

be integrated with 3D seismic interpretation. Thereby, we can link Q estimates with anomalies related to the presence of gas hydrate and free gas in the sediments.

STUDY AREA

Our study focuses on the active seeping segment of Vestnesa Ridge, a ~100 km long gas hydrate charged contourite drift developed over < 20 Ma oceanic crust offshore west-Svalbard (Figure 1) (Eiken and Hinz, 1993; Vogt et al., 1994, Bünz et al., 2012). The contourite drift is in close proximity to the Molloy and the Knipovich slow-spreading oceanic ridges and it is located between the Molloy and the Spitsbergen Transform Faults (e.g., Ritzmann et al., 2004). Vestnesa Ridge consists of three main stratigraphic sequences named according to correlation with ODP sites at the Yermak Plateau (YP) (Eiken and Hinz, 1993): the oldest unit (YP1) is of Miocene age and consists dominantly of syn-rift deposits directly lying over the oceanic crust (Eiken and Hinz, 1993; Ritzmann et al., 2004); the middle sequence (YP2) consists of sediments deposited by migrating contour currents; and finally the youngest sequence (YP3), is dominated by margin parallel contour currents and by glacigenic debris flow deposits (Howe et al., 2008).

A gas hydrate system and associated free gas zone exists along Vestnesa Ridge (Hustoft et al., 2009; Petersen et al., 2010; Bünz et al., 2012; Plaza-Faverola et al., 2015). The system is restricted to the upper stratigraphic sequence (YP3) and has a series of gas chimneys and pockmarks associated along the full extent of Vestnesa Ridge. However, only pockmarks located towards the easternmost part of the ridge (where our 3D seismic survey is located; Figure 1) are actively seeping gas at present (Bünz et al., 2012; Smith et al., 2014). Gas chimneys towards the westernmost part of the ridge seem inactive at present but foraminiferal records indicated past activity at around 8000 my ago (Consolaro et al., 2014).

140 DATA

141 We used high-resolution P-Cable (Planke et al., 2009; Petersen et al., 2010) 3D
142 seismic data acquired in 2013 on board R/V Helmer Hanssen (Plaza-Faverola et al., 2015).
143 The system consists of 14 streamers towed parallel behind the ship. The 25-m-long streamers
144 contain 8 receiver groups each. The streamers are attached to a cross cable towed
145 perpendicular to the vessel's streaming direction and spread by two large trawl doors. The
146 spacing of streamers along the cross cable is 12.5 m. However, due to curvature of the cross
147 cable, the distance between streamers is varying between 6-10 m. The high-resolution P-
148 Cable system was used together with mini-GI gun (15/15 in^3). The gun was fired at an
149 interval of 6 s with a firing pressure of 170 bar. Source-receiver offset varies from 97-143 m.
150 Traces have been recorded with 3 s record length at 0.25 ms sampling interval.

151 During seismic data processing, utmost care has been taken to avoid all the steps that
152 can potentially distort the amplitude spectrum within the main seismic bandwidth. The
153 processing of the high-resolution 3D seismic data mainly included navigational correction,
154 static and tidal correction, binning, bandpass filtering (10-20-300-350), NMO correction and
155 stacking. NMO correction can potentially distort the amplitude spectrum due to NMO
156 stretching. But for short offset seismic data in deep water, this distortion will be too small and
157 can be neglected. 3D Stolt migration was applied using a constant velocity of 1500 m/s. The
158 spatial resolution of the seismic data is quite high with a bin size of 6.25 x 6.25 m. The
159 seismic data covers an area of about 14 km^2. The data has a broad frequency spectrum
160 ranging from approximately 20 to 300 Hz (Figure 2a).

161

METHODOLOGY

Amplitude, frequency and phase are three basic attributes of a seismic signal. Quantitative analysis of these attributes is done using different derivations and transforms. For example, quantitative estimation of frequency attribute involves different time-frequency transforms. Reine et al. (2009) discussed the robustness of seismic attenuation measurements using different time-frequency transforms. In the present study, short-time Fourier transform (Gabor, 1946) is used to transform a seismic signal into frequency domain. The data converted to frequency domain is used to study seismic attenuation. We use centroid frequency shift (Quan and Harris, 1997) and spectral ratio method (Jannsen et al., 1985) to estimate Q in gas hydrate and free gas saturated sediments.

Centroid frequency method

Centroid frequency of an amplitude spectrum (f_c) is defined as:

$$f_c = \frac{\sum A(f)\, x\, f}{\sum A(f)} \quad (1)$$

Where A(f) corresponds to amplitude of frequency (f) in an amplitude spectrum.

Centroid frequency of a signal gives an idea about the energy level of a signal. Since energy of a signal decreases as it propagates in the sub-surface, centroid frequency of an amplitude spectrum shifts towards lower values with further propagation into deeper layers. By plotting the centroid frequency for the entire seismic section, a broad overview about the subsurface seismic attenuation can be established. Quan and Harris (1997) proposed a method to estimate Q using centroid frequency shift analysis. They considered the amplitude spectrum of the received signal R(f) as a function of incident wave S(f) and instrument/medium response G(f)H(f).

$$R(f) = G(f)H(f)S(f) \quad (2)$$

Parameter G(f) includes geometrical spreading, instrument response, source/receiver coupling, radiation/transmission coefficients, and phase accumulation effects caused by propagation. H(f) is a factor which takes into account the effect of intrinsic attenuation on a seismic signal. Since attenuation is proportional to frequency within the seismic bandwidth, response H(f) can be written as (Johnston et al., 1979):

$$H(f) = \exp\left(-f\int_{ray}\alpha_0 dl\right) \quad (3)$$

Where the integral is taken along the ray path, and α_0 is the attenuation coefficient defined by (Johnston et al., 1979):

$$\alpha_0 = \frac{\pi}{Qv} \quad (4)$$

Where Q is the quality factor and v is the velocity of the medium.

With the assumption that the amplitude spectrum follows Gaussian pattern of distribution, Quan and Harris (1997) after rearranging the equations finally came to the following equation:

$$\int_{ray}\alpha_0 dl = \frac{f_s - f_r}{{\sigma_s}^2} \quad (5)$$

Where f_s is the centroid frequency of the source signal (Figure 2b), f_r is the centroid frequency of the received signal, and ${\sigma_s}^2$ is the variance of the source amplitude spectrum.

$${\sigma_s}^2 = \frac{\int_0^\infty (f - f_s)^2 A(f) df}{\int_0^\infty A(f) df} \quad (6)$$

Where A(f) is the amplitude spectrum of the source signal and other parameters are same as described in the above equation. In order to account for the increase in the variance of amplitude spectrum, σ_s^2, of seismic signal with arrival time, a trend line for σ_s^2 at different arrival times is estimated (Figure 2c). Straight line is fitted to the mean σ_s^2 values.

If velocity and quality factor (Q) is assumed constant in a medium, the final expression for quality factor (Q) can be written (Talukder, 2013) as:

$$Q = \frac{\pi \sigma_s{}^2 \Delta t}{f_s - f_r} \quad (7)$$

Where Δt is the total travel time and rest of the parameters are same as described in above equations.

Spectral ratio method

Spectral ratio method is one of the most commonly used methods to estimate Q in a medium. This method takes into account the differential decay of different frequencies. Higher frequencies tend to decay at a much higher rate as compared to lower frequencies while passing through an attenuating medium (Båth, 1982). Differential decay of different frequencies depends upon Q of a medium.

Jannsen et al. (1985) discussed about the application of spectral ratio method to estimate Q from seismic data. Amplitude spectrums ($A_1(\omega)$ and $A_2(\omega)$) of two reflections from different depths (Z_1 and Z_2), can be written as:

$$A_1(\omega) = A_0(\omega) G(Z_1) R_1 e^{-2\alpha_1 Z_1} \quad (8)$$

$$A_2(\omega) = A_0(\omega) G(Z_2) (1 - R_1{}^2) R_2 e^{-2\alpha_1 Z_1} e^{-2\alpha_2 (Z_2 - Z_1)} \quad (9)$$

Where $A_0(\omega)$ is the amplitude spectrum of the incident wavelet at Z=0, $G(Z_1)$ and $G(Z_2)$ accounts for the geometrical spreading and other factors leading to decay in amplitudes, R_1 and R_2 are reflection coefficients for different boundaries, and α_1 and α_2 are the attenuation coefficients. The spectral ratio (SR) of two spectra can be written as:

$$SR(\omega) = C_1 e^{-2\alpha_2(Z_2 - Z_1)} \qquad (10)$$

$$C_1 = \frac{G(Z_2)(1-{R_1}^2)R_2}{G(Z_1)R_1} \qquad (11)$$

Where C_1 is the ratio of factors related to geometrical spreading and reflection coefficients. Assuming phase velocity β to be independent of frequency in spectral ratio (Båth, 1982), natural log of spectral ratio can be written as:

$$\ln\big(SR(\omega)\big) = \ln(C_1) - \alpha_2 \Delta T \beta \qquad (12)$$

where ΔT is the time difference between two reflections. Substituting the value of α as $\pi f/(Q\beta)$ (Johnston et al., 1979), we get linear relation between ln (SR(ω)) and frequency, i.e.,

$$\ln\big(SR(\omega)\big) = \ln(C_1) - \left(\frac{\pi \Delta T}{Q}\right) f \qquad (13)$$

Hence, the slope i.e. - ($\pi\Delta T/Q$) of the spectral ratio (in logarithmic scale) vs frequency plot depends on the Q of a medium, and the intercept is related to the geometrical spreading and reflection coefficients which are independent of frequency. Using this concept, Q value can be estimated from the slope of the best fit line in spectral ratio (in logarithmic scale) vs frequency plot. In real data, two wavelets can be picked by windowing two reflections (Figure 3a) and then Fourier transform can be applied to get amplitude spectrum of these two

wavelets (Figure 3b). Spectral ratio method can be applied on these two amplitude spectrums and effective Q of a medium between these reflections can be estimated (Figure 3c).

ANALYSIS USING CENTROID FREQUENCY METHOD

Analysis using centroid frequency plots has been done to study changes in the centroid frequency with depth. An inline has been selected from seismic data where a BSR is clearly identified by high-seismic amplitudes at about 1.9 s TWT in the seismic section (Figure 4a) (Bünz et al., 2012; Smith et al., 2014). The BSR separates hydrate-bearing sediments from a ~100 m thick free gas zone (Hustoft et al., 2009). Other notable features are vertical zones of acoustic transparency or chaotic seismic facies. These are interpreted as vertical fluid-flow features, so-called chimneys. They terminate in seafloor depressions known as pockmarks (Figure 4c) (Bünz et al., 2012).

The centroid frequency has been calculated for all the traces in the seismic section at an interval of 5 ms. Enough samples have been taken to ensure that the lowest frequency in the main seismic bandwidth will have at least one wavelength to sample. The derived centroid frequencies are shown in Figure 4b. The centroid frequency decreases significantly beneath the BSR. Prominent low centroid frequency anomalies are observed in the free gas zone especially in the southeastern part of the seismic section (Figure 4b). Gas chimneys are observed in the seismic section. Some gas chimneys also show low centroid frequency anomalies. Some of these anomalies appear to intrude the chimneys from the free gas zone beneath the BSR. Coincidentally, intrusion happens for gas chimneys that have active gas seepage at the seafloor (Figure 4c) (Bünz et al., 2012).

Q estimation

Variance of an amplitude spectrum (σ_s^2) and reference centroid frequency (f_s) were calculated to further estimate Q for different layers using centroid frequency shift method. In order to account for an increase in the σ_s^2 with arrival time, σ_s^2 of a seismic signal is plotted with respect to two-way arrival time. The trend line for σ_s^2 at different arrival times is estimated (Figure 2c). The σ_s^2 to be used in equation (7) is calculated from the linear fit parameters of the best fit line. The centroid frequency of a seismic signal at the sea floor is used as a reference centroid frequency for estimating 1-D Q model for every trace. The centroid frequency of the seismic signal in shallow sediments close to the seafloor (shown in Figure 2b) ranges from 150-185 Hz for almost all the traces except for few located in a pockmark where it showed lower centroid frequency values. The centroid frequency of the seismic signal at the seafloor is expected to be higher than the centroid frequency of a seismic signal in shallow sediments. After neglecting aberrations, we use 182 Hz as a reference centroid frequency (Figure 2b).

Prominent reflections observed in the seismic data have been picked and Q values for different layers between picked reflections have been estimated (Figure 5a and 6a). Q model derived from one of the traces in the seismic data is shown in Figure 5a-d. Centroid frequencies are calculated at a time interval of 5 ms for each trace using a sliding time window along the trace (Figure 5a-b). Fluctuations in centroid frequencies make Q estimation difficult. Therefore, in order to reduce these effects, centroid frequencies of traces falling within 31.25 x 31.25 m^2 bin have been stacked to get a centroid frequency trend/curve (Figure 5c). This process also reduces the size of the seismic dataset and makes it computationally convenient. Synthetic centroid frequency curves are generated for different possible Q models (Q varying from 1 to 600 in all the 5 layers). Synthetic centroid frequency

curves for 5 Q models out of 600^5 possible Q models are shown in green color in Figure 5d. These synthetic centroid frequency curves are matched with estimated centroid frequency curves (estimated from traces in 31.25 x 31.25 m^2 bin), and the misfit between the two curves has been computed. The L_1 norm approach (Claerbout and Muir 1973) has been used to calculate the misfit and to pick the best possible Q model out of the possible range of Q models. The L_1 norm approach has been adopted to reduce the significance of the spiky points in the centroid frequency curves. This process of estimating Q has been repeated on all the traces in the seismic data to generate a Q cube.

Observations

The Q values along one of the inlines (Figure 6a) indicate high Q anomalies in the layer above the BSR and low Q anomalies below the BSR (Figure 6b). Q slices for different layers give an idea about the lateral variation of Q within a layer. Figure 7 shows Q slices for different layers illustrating the lateral variation of Q anomalies within a layer. The BSR lies between Q slices in Figure 7c and 7d. We observe particularly low Q values in some areas within the first layer (Figure 7a) coinciding with the location of the chimney structures. Q estimates in the second layer follows a normal trend except for few small patches of high Q (Figure 7b). Some of these slightly elevated Q values seem to correspond particularly with the outer rims of the chimney structures (Figure 7b). Just above the BSR, we observe very high Q values, particularly in the southern half of the 3D seismic data (Figure 7c). These anomalies are found to be laterally continuous. On the contrary, Q values in the center part of this slice (Figure 7c) follow the trend of chimneys and Q values are comparatively lower than those in the slice above (Figure 7b). Extremely low Q values have been observed in Q slice corresponding to free gas zone beneath the BSR except for the locations corresponding to that of chimneys (Figure 7d).

ANALYSIS USING SPECTRAL RATIO METHOD

Q estimation

The spectral ratio method can be applied to estimate effective Q of a medium between two prominent reflections (Figure 3). We extend this method to estimate Q for the same 4 layers between prominent reflections in the seismic data (Figure 6a) as used in centroid frequency shift method. Picked reflections are windowed and spectral ratio method is applied on adjacent reflections to estimate a subsurface Q model. Figure 8 shows different steps involved in the application of the spectral ratio method on one of the traces. The same procedure is repeated on all the traces in the seismic volume to generate a Q cube.

Observations

The Q pattern for one of the inlines (Figure 6a) shows high Q values in the layer just above the BSR (Figure 6c). Q estimates based on spectral ratio method in this layer (Figure 6c) is comparable to the Q estimates from centroid frequency shift method (Figure 6b). Q slices for different layers are plotted to further analyze the results (Figure 9). In the plan view, Q estimates vary significantly within the first layer (Figure 9a). In the second layer, small patches of high Q values coincide with the chimney features similar to that obtained by centroid frequency shift method. Also, we observe high Q anomalies in the Q slice corresponding to the layer just above the BSR (Figure 9c). We find that these high Q anomalies are laterally continuous and match well with the anomalies observed in Q slice obtained from centroid frequency shift method (Figure 7c). Beneath the BSR, we observe predominantly low Q values (Figure 9d). However, we also observe some regions with high Q anomalies in the fourth layer roughly corresponding to chimney locations (Figure 9d). Here, results obtained through spectral ratio method (Figure 9d) and centroid frequency shift

335 method (Figure 7d) do not agree with each other. At the BSR depth, signal strength is
336 significantly reduced and Q estimates from spectral ratio method are extremely unstable. This
337 may be the reason for high Q values observed in some areas below the BSR.

338 ## UNCERTAINITIES AND LIMITATIONS

339 Estimating Q from seismic data is typically accompanied by some uncertainties and
340 limitations. Contribution of reflectivity sequences in calculated amplitude spectrum directly
341 affects Q estimates. In case of thin layers with some periodicity, Earth's reflectivity function
342 contributes in shaping the spectrum of effective recorded signals. Weak reflectivity over a
343 time window (Figure 5a) can also create bias in Q estimates if the noise spectrum is not
344 white. Ning and Wen-kai (2010) discussed in detail about the effect of reflectivity sequences
345 on Q estimates. Spectral ratio method is more sensitive to these effects as Q is estimated from
346 the spectrum of two wavelets. Fluctuations observed in centroid frequency curves is also
347 primarily due to the effect of reflectivity sequences in the recorded signal.

348 Scattering is another factor that will lead to reduction in amplitude of different
349 frequencies. Different types of scattering can occur depending on the size of the particles
350 which include Rayleigh, Mie and forward scattering (Mavko et al., 1998). Mie scattering is
351 the type of scattering that will occur when the heterogeneity scale length is of the order of the
352 seismic wavelength. The main difference between scattering and intrinsic attenuation is that
353 scattering redistributes wave energy within the medium but does not remove the energy from
354 the overall wavefield whereas intrinsic attenuation converts vibration energy into heat energy
355 (Sato and Fehler, 1997). Intrinsic attenuation quantified using different methods also includes
356 the contribution from scattering attenuation (Spencer et al., 1982). This will directly affect the
357 Q estimates from different methods.

Processing of seismic data can be another source of error in Q estimation. Ideally, all the processing steps which can potentially alter amplitude spectrum of a seismic signal should be avoided. In P-Cable data, the potential of this problem is significantly reduced as P-Cable data is close to zero offset (97-143 m), particularly given the water depth in the present study. Frequency distortions due to NMO stretching are negligible for small offsets at deep water depths. Frequency distortions due to Stolt migration are also negligible as layers in the study area are essentially flat. Apart from these two processing steps, no other step has been involved which can potentially influence the analysis.

Travel time through a picked layer is a very important factor in estimating Q using centroid frequency shift method. Picking more reflections and using them as layer boundaries increases the number of layers for which effective Q model will be estimated but decreases the travel time of the layers. Effect of fluctuations in the centroid frequency curve on Q estimates is more pronounced for thinner layers. Thus, accuracy of Q estimates in thinner layers is poorer than thicker layers. Figure 5e shows best fit Q models for different number of layers. When the number of picked layers is increased from 5 to 7, the instability in the Q estimates can be clearly seen. Therefore, reflections need to be picked properly so that Q can be estimated for different layers with an acceptable accuracy.

Histogram of Q estimates from centroid frequency shift method (Figure 10a) and spectral ratio method (Figure 10d) in layer 3 (which lies just above the BSR) have been plotted to analyze the statistical distribution of Q estimates within a layer. The peak at Q=600 observed in the histograms is due to the fact that only Q values up to 600 have been taken into consideration. All Q values greater than 600 will be estimated as 600 and it is extremely difficult to differentiate between different Q values for those higher than approximately 150. Accuracy of Q estimates decreases for high Q values where it changes very rapidly with

small change in seismic signal decay. This small amount of decay becomes comparable with the fluctuations caused by other factors which create a problem in Q estimation. Figure 5d shows the estimated Q for different layers. From layer 2 to layer 3, estimated Q changes from 160 to 403, but there is a very small change in tilt of the best fit curve. This limits the accuracy of Q estimates for high Q values and due to this fact, only Q values up to 600 have been taken into consideration (Figure 10).

Given the two methodological approaches for estimating Q, their inherent limitations and the constraints of the 3D seismic, as earlier reported by Quan and Harris (1997) and Matsushima (2006), we also found that the centroid frequency shift method gave more stable Q estimates. Contribution of reflectivity sequences in calculated amplitude spectrum and scattering effects limited the vertical resolution of Q estimates. We tried to do high-resolution Q sampling but accuracy of Q estimates decreased when greater number of layers was used to estimate Q. Reflectivity sequences and scattering effects made the continuous mapping of Q unstable. Q estimates became unreliable for thinner layers. We observed trade-off between the accuracy and resolution.

DISCUSSION

There are different factors which contribute to intrinsic attenuation of a seismic signal (Toksöz and Johnston, 1981). Major factors which play a crucial role are lithology, fluid type and structural features (Walsh, 1966; Johnston et al., 1979; Toksöz et al., 1979; Toksöz and Johnston, 1981; Winkler et al., 1979; Spencer, 1979; Winkler and Nur, 1982; Murphy et al., 1986; Pointer et al., 2000; Parra et al., 2002; Prasad and Nur, 2003; Behura, 2009). The exact details of the sedimentary environment of the study area are not well known but it is believed to be composed of smoothly deposited layers of contourite deposits (Eiken and Hinz, 1993; Howe et al., 2008). Under such geological settings, the major factors which can prominently

406 change the intrinsic attenuation property of a medium are changes in fluid type and fluid
407 saturation. Changes in gas hydrate saturation within gas hydrate stability zone will sharply
408 change the intrinsic attenuation spatially. Several publications explained the relationship
409 between seismic attenuation and fluid saturation (O'Connell and Budiansky, 1977; Mavko
410 and Nur, 1979; Spencer, 1979; Murphy et al., 1986; O'Hara, 1989; Pointer et al., 2000;
411 Prasad and Nur, 2003; Rapoport et al. 2004). In addition, structural features scatter the
412 seismic signal and contribute significantly to the estimated intrinsic attenuation (Hamilton
413 and Mooney, 1990). It is thus challenging to distinguish between scattering attenuation and
414 intrinsic attenuation (Wennerberg, 1993). The Q parameter estimated for quantifying intrinsic
415 attenuation of a medium also includes the effects from scattering attenuation (Spencer et al.,
416 1982). Possible effects of gas hydrates and free gas on Q estimates is studied by estimating Q
417 values for different layers in the gas hydrate stability zone and free gas zone. The spatial
418 analysis of the Q estimates from the 3D seismic data then allows us to recognize structures
419 and areas that can be related to the presence of gas hydrates in marine sediments even in the
420 absence of seismic velocity control.

421 Q values have been estimated for different layers using centroid frequency shift
422 method and spectral ratio method. Q values estimated in deeper layers (L2, L3, and L4) using
423 these two methods are found to be in concordance with each other and Q values in layers just
424 above the BSR (L2 and L3) are in good agreement with the Q values normally observed in
425 the gas hydrate bearing marine sediments (Wood et al., 2000). Q estimates in the first layer
426 (L1) do not correspond well. Noisy amplitude spectrum near the sea floor (Dewangan et al.
427 2014) and fluctuating spectral ratio (Figure 8c) can be the possible reason for the unstable Q
428 estimates from spectral ratio method in the first layer. However, in the context of this
429 analysis, it is important to study relative changes in Q particularly along Q slices throughout

the whole volume as these might be related to the type of pore fluid and saturation in a given area or structure.

Both Q analysis methods estimate high Q values in a layer just above the BSR (Figure 7c and Figure 9c). Below the BSR, the centroid frequency (Figure 4b) and Q values of both methods drop significantly (Figure 7d and Figure 9d). Very low Q values are observed below the BSR except for the locations below chimneys, where high Q is observed (Figure 7d and Figure 9d). High free gas concentration can be the reason for rapid attenuation of the seismic signal below the BSR. The strength of the BSR in the seismic data (Figure 4a) also gives some indication about the accumulation of free gas in the region which is estimated to be as high as 1.5-2% of pore space (Hustoft et al., 2009). In gas chimneys, seismic signal significantly attenuates due to scattering especially in shallow seafloor features like pockmarks. Low signal strength accompanied with seismic blanking in the gas chimneys make Q estimates in gas chimneys unreliable especially at deeper depths.

By analyzing the distribution of Q values in the layer L3 (Figure 10a and 10d), it can be stated that the background Q values in the marine sediments at the BSR depth is in the range of 60-90. If Q values in the layer L3 (layer above the BSR) above potentially gas saturated sediments ($Q<30$ below the BSR in the layer L4) are selectively picked (Figure 10b and 10e) and compared with the overall distribution of Q values in the layer (Figure 10c and 10f), relatively higher Q values have been observed above potentially gas saturated sediments (Figure 10). Particularly the variable distribution of extended zones of high Q mapped on Q slices of the 3D data (Figure 11b), in comparison to adjacent areas with lower Q, points towards variable pore fluid type and/or saturation in this strata. There is no indication from the seismic data to expect significant lithologic changes in this rather homogeneous sedimentary environment. Therefore, we attribute this effect to the presence of gas hydrates

in the sediments and suggest that gas hydrate saturated sediments exhibit high Q values within the frequency range used in the study. This observation is supported by the fact that both Q analysis methods match well in the distribution of Q above the BSR. In contrast, areas with very low Q below the BSR indicate the presence of free gas (Figure 11c).

It is difficult to estimate accurate Q for high Q value areas as discussed earlier. Therefore it becomes difficult to state exact Q value in gas hydrate saturated sediments. But from the statistical analysis of the results obtained from both methods (Figure 10), it can be stated that high Q values are observed in gas hydrate saturated sediments. Earlier studies on seismic attenuation conducted in the nearby locations also indicated elevated Q values above the BSR (Rossi et al., 2007). Hence, we argue that Q analysis of high-resolution P-Cable 3D seismic data with a large bandwidth can detect and outline spatially limited areas of gas hydrate occurrence in marine sediments.

Hustoft et al. (2009) used 135 km east-west striking multi-channel seismic (MCS) profile to derive a velocity model. This profile lies approximately 10 Km southward to our study area (shown in Figure 1) and can be used to interpret the results of the Q analysis. High gas concentrations exist beneath the BSR towards the southwestern half of the Vestnesa Ridge (Hustoft et al., 2009). Similarly, low Q values beneath the BSR in the southwestern half of the 3D seismic data may indicate the presence of elevated gas concentrations at this location (Figures 7d and 9d). The gas chimneys that align at the crest of the Vestnesa Ridge separate this southwestern half from the northeastern half where Q values are generally higher. A similar behavior is observed above the BSR where high Q values in the southwestern half may indicate higher concentrations of gas hydrates than in the northeastern half. Hustoft et al. (2009) and Bünz et al. (2012) showed that the fluid flow system in the Vestnesa Ridge is topographically controlled and that gas migrates to the crest of the ridge

beneath the BSR, mostly from the southwestern half. Hence, gas availability may be higher in the southwestern half.

In a more recent study, Plaza-Faverola et al. (2015) showed that small-scale fault systems exist at the crest of the Vestnesa Ridge documenting a tectonic control of gas leakage. Fault systems mapped by Plaza-Faverola et al. (2015) at approximately the BSR depth coincide strikingly with the boundaries of abrupt Q changes within layer 3 and 4 above and beneath the BSR, respectively (Figure 11a-c). Changes in Q within a layer are attributed with a variable pore fluid fill. Hence, the Q analysis indicates that fluid distribution in the region is strongly controlled by fault systems in the Vestnesa Ridge. Fault 1 in Figure 11a delimits the southwestern part indicating higher fluid concentrations in both hydrates above the BSR and free gas below. This area also includes the two most active chimneys on the Vestnesa Ridge (Figure 4c) (Bünz et al., 2012; Smith et al., 2014) corroborating our results that gas is more readily available at this location to either leak to the seafloor or to be bound into gas hydrates. As gas migrate upslope in north-east direction (Figure 11d; Hustoft et al., 2009), they are trapped by the regional fault 1 and utilize the fault plane as migration pathway into the free gas zone beneath the BSR.

Q values between fault 1 and 2 indicate lower concentrations of gas hydrates (Figure 11b) and free gas (Figure 11c). Coincidentally, several of the chimneys located in this fault block are inactive. The reduced availability of free gas in this fault block might explain this observation or that most gas has vented through the chimneys. Also other areas of the 3D seismic volume clearly indicate a relationship between Q values and the mapped fault system, e.g. to the northeast of fault 2 or between fault 2 and fault 4 (Figure 11a-c). Together, these results suggest that the availability of free gas is one of the major factors in the accumulation of gas beneath the BSR and the formation of gas hydrates above it, and that the availability of

free gas clearly seems to be controlled by the structural setting supporting the findings of Plaza-Faverola et al. (2015).

All the Q slices clearly exhibit the vertical fluid flow features in this area (Figures 7 and 9). However, there are still some interesting subtleties that can be noted from the Q data. When centroid frequencies are plotted for a seismic section, they didn't drop rapidly at some places in the northwestern and central parts (Figure 4b) of the seismic section. It is possible that these frequency anomalies might be related to variable concentrations of gas within the free gas zone beneath the BSR. Lower amounts of free gas might indicate that the fluid flow features like gas chimneys in nearby locations may lack a gas source. Bünz et al. (2012) documented acoustic flares in the water column and shallow high amplitudes in upper 50 m of these fluid flow features. In their study they show that the chimneys in the central part of the 3D seismic volume and some chimneys in northwestern part are inactive as compared to chimneys in the southeastern part of the volume (Figure 4c). On the contrary, the active chimneys documented by Bünz et al. (2012) show low frequency anomalies in the lower part of the chimney just above the BSR (Figure 4b). It might indicate an active migration of gas from the free gas zone into the chimney structures supplying the seafloor seep with gas.

Low centroid frequencies have been observed in regions where pockmark features have been observed. This can be due to prominent scattering at pockmarks or attenuation of the seismic energy within 5-10 m of sediments below the sea floor possibly resulting from the presence of hydrates and/or carbonates. Prominent scattering in pockmarks and within chimneys significantly reduced the signal strength and made it difficult to image Q in gas chimneys at deeper depth. Low signal strength and seismic blanking in gas chimneys reduces the accuracy of Q estimates in gas chimneys. But still Q values with limited accuracy have been used to study gas chimneys. Both Q estimation methods show small patches of high Q

values associated with chimney features at medium depth beneath seafloor and BSR (Figure 7b and Figure 9b). However, the centroid frequency shift method depicts high Q at the rim of the chimneys possibly indicating that chimneys are lined with hydrates, an interesting though speculative suggestion, although it would fit with theoretical models for chimneys structures (Liu and Flemings, 2007).

SUMMARY

We applied the centroid frequency shift method and spectral ratio method to study seismic attenuation in gas hydrate and free gas saturated sediments using high-resolution P-Cable 3D seismic data from Vestnesa Ridge on the Arctic continental margin of Svalbard. We estimated Q values for different layers to develop a subsurface 3D Q model. We observed high Q values above the prominent BSR and low Q values ($Q \approx 10\text{-}30$) below the BSR. Anomalies observed in Q slices obtained from two different methods are found in concordance with each other. But we got relatively more stable Q values from centroid frequency shift method.

After performing a statistical analysis, we found that an increase in Q values in certain, spatially limited areas above the BSR can probably be associated with the presence of gas hydrates. Under this premise, Q analysis of high-resolution P-Cable 3D seismic data is thus an effective method for the detection and mapping of gas hydrate occurrences in marine sediments. Q values estimated for the strata below the BSR are very low as a consequence of the occurrence of gas trapped in the free gas zone beneath hydrate-bearing strata.

Faults that exist throughout the Vestnesa Ridge coincide with the Q anomalies in the layers above and below the BSR corroborating recent findings and directly showing that the structural setting and tectonic activity in the region control the availability and spatial

549 distribution of free gas and gas hydrates in the Vestnesa Ridge. The availability of gas in
550 certain spatially limited areas also might explain the present seepage from some of the
551 chimneys on the Vestnesa Ridge whereas other chimneys are dormant. Low seismic signal
552 strength accompanied by amplitude blanking makes it difficult to accurately image Q in gas
553 chimneys. But still with limited accuracy, we observed high Q values in gas chimneys in Q
554 slices hinting towards the presence of gas hydrates in gas chimneys.

555 ## ACKNOWLEDGEMENTS

556 This work is partly supported by the Research Council of Norway through its Centres
557 of Excellence funding scheme, project number 223259. We thank the crew of R/V Helmer
558 Hanssen and those who contributed to P-Cable data acquisition. We are also thankful to Ingo
559 Pecher (Associate Editor), Nathan Bangs, Giuliana Rossi, and Kalachand Sain for their
560 constructive comments.

561 ## REFERENCES

562 Amundsen, L., and R. Mittet, 1994, Estimation of phase velocities and Q-factors from
563 zero-offset, vertical seismic profile data: Geophysics, **59**, 500– 517.

564 Badri, M., and H. M. Mooney, 1987, Q measurements from compressional seismic
565 waves in unconsolidated sediments: Geophysics, **52**, 772– 784.

566 Båth, M., 1982, Spectral Analysis in Geophysics: Elsevier Science.

567 Bauer, K., C. Haberland, R. G. Pratt, F. Hou, B. E. Medioli, and M. H. Weber, 2005,
568 Ray based cross-well tomography for P-wave velocity, anisotropy, and attenuation structure
569 around the JAPEX/JNOC/GSC et al. Mallik 5L-38 gas hydrate production research well, *in* S.
570 R. Dallimore, and T. S. Collet, eds., Scientific results from the Mallik 2002 Gas Hydrate

571 Production Research Well Program, Mackenzie Delta, Northwest Territories, Canada:
572 Geological Survey of Canada, Bulletin 585, 1-21.

573 Behura, J., 2009, Estimation and Analysis of Attenuation Anisotropy: Doctoral thesis,
574 Colorado School of Mines.

575 Bellefleur, G., M. Riedel, T. Brent, F. Wright, and S. R. Dallimore, 2007, Implication
576 of seismic attenuation for gas hydrate resource characterization, Mallik, Mackenzie Delta,
577 Canada: Journal of Geophysical Research, **112**, B10311, doi:10.1029/2007JB004976.

578 Best, A. I., J. A. Priest, C. R. I. Clayton, and E. V. L. Rees, 2013, The effect of
579 methane hydrate morphology and water saturation on seismic wave attenuation in sand under
580 shallow sub-seafloor conditions: Earth and Planetary Science Letters, **368**, 78-87.

581 Brooks, J. M., H. B. Cox, W. R. Bryant, M. C. Kennicutt II, R. G. Mann, and T. J.
582 McDonald, 1986, Association of gas hydrates and oil seepage in the Gulf of Mexico: Organic
583 Geochemistry, **10**, 221-234, doi: 10.1016/0146-6380(86)90025-2.

584 Bünz, S., S. Polyanov, S. Vadakkepuliyambatta, C. Consolaro, and J. Mienert, 2012,
585 Active gas venting through hydrate-bearing sediments on the Vestnesa Ridge, offshore W-
586 Svalbard: Marine Geology, **332-334**, 189-197, doi:10.1016/j.margeo.2012.09.012.

587 Chand, S., and T. A. Minshull, 2004, The effect of hydrate content on seismic
588 attenuation: a case study for Malik 2L-38 well data, Mackenzie delta, Canada: Geophysical
589 Research Letters, **31**, L14609, doi:10.1029/2004GL020292.

590 Chand, S., T. A. Minshull, D. Gei, and J. M. Carcione, 2004, Elastic velocity models
591 for gas-hydrate bearing sediments – A comparison: Geophysical Journal International, **159**,
592 573-590.

593 Claerbout, J. F., and F. Muir, 1973, Robust modeling with erratic data: Geophysics,
594 **38**, 826-844.

595 Collett, T. S., and J. Ladd, 2000, Detection of gas hydrate with downhole logs and
596 assessment of gas hydrate concentrations (saturations) and gas volumes on the Blake Ridge
597 with electrical resistivity log data, *in* C. K. Paull, R. Matsumoto, P. J. Wallace, and W. P.
598 Dillon, eds., Proceedings of the Ocean Drilling Program, Scientific results: Texas A & M
599 University, College station Texas, **164**, 179-191.

600 Collet, T. S., R. E. Lewis, S. R. Dallimore, M. W. Lee, T. H. Mroz, and T. Uchida,
601 1999, Detailed evaluation of gas hydrate reservoir properties using JAPEX/JNOC/GSC
602 Mallik well 2L-38 gas hydrate research well downhole well-log displays, *in* S. R. Dallimore,
603 T. Uchida, and T. S. Collett, eds., Scientific Results from JAPEX7JNOC/GSC Mallik 2L-38
604 gas hydrate well, Mackenzie Delta, North west Territories, Canada, Geological Survey of
605 Canada Bulletin 544, 295-312.

606 Consolaro, C., T. L. Rasmussen, G. Panieri, J. Mienert, S. Bünz, and K. Sztybor,
607 2014, Carbon isotope ($\delta^{13}C$) excursions suggest times of major methane release during the
608 last 14 ka in Fram Strait, the deep-water gateway to the Arctic: Climate of the Past
609 Discussions, **10**, 4191-4227, doi:10.5194/cpd-10-4191-2014.

610 Dewangan, P., R. Mandal, P. Jaiswal, T. Ramprasad, and G. Sriram, 2014, Estimation
611 of seismic attenuation of gas hydrate bearing sediments from multi-channel seismic data: A
612 case study from Krishna–Godavari offshore basin: Marine and Petroleum Geology, **58**, Part
613 A, 356-367, doi:10.1016/j.marpetgeo.2014.05.015.

614 Ecker, C., J. Dvorkin, and A. Nur, 1998, Sediments with gas hydrates: Internal
615 structure from seismic AVO: Geophysics, **63**, 1659-1669.

Eiken, O., and K. Hinz, 1993, Contourites in the Fram Strait: Sedimentary Geology, **82**, 15-32.

Gabor, D., 1946, Theory of communication: Journal of the Institution of Electrical Engineers, **93**, no. 26, 429–457.

Galperin, E. I., 1985, Vertical seismic profiling and its exploration potential: Springer, doi: 10.1007/978-94-009-5195-2.

Gei, D., and J. M. Carcione, 2003, Acoustic properties of sediments saturated with gas hydrate, free gas and water: Geophysical prospecting, **51**, 141-157.

Gladwin, M. T., and F. D. Stacey, 1974, Anelastic degradation of acoustic pulses in rocks: Physics of the Earth and Planetary Interiors, **8**, 332– 336.

Guerin, G., and D. Goldberg, 2002, Sonic waveform attenuation in gas hydrate-bearing sediments from the Mallik 2L-38 research well, Mackenzie Delta, Canada: Journal of Geophysical Research, **107**, no. B5, 2088, doi:10.1029/2001JB000556.

Guerin, G., and D. Goldberg, 2005, Modeling of acoustic wave dissipation in gas hydrate–bearing sediments: Geochemistry, Geophysics, Geosystems, **6**, Q07010, doi:10.1029/2005GC000918.

Guerin, G., D. Goldberg, and A. Meltser, 1999, Characterization of in situ elastic properties of gas hydrate bearing sediments on the Blake Ridge: Journal of Geophysical Research, **104**, 17781-17795.

635 Hamilton, R. M., and W. D. Mooney, 1990, Seismic-wave attenuation associated with
636 crustal faults in the new madrid seismic zone: Science, **248**, no. 4953, 351-354,
637 doi: 10.1126/science.248.4953.351.

638 Hatherly, P. J., 1986, Attenuation measurements on shallow seismic refraction data:
639 Geophysics, **51**, 250– 254.

640 Howe, J. A., T. M. Shimmield, and R. Harland, 2008, Late Quaternary contourites
641 and glaciomarine sedimentation in the Fram Strait: Sedimentology, **55**, no.1, 179-200.

642 Hustedt, B., and R. A. Clark, 1999, Source/receiver array directivity effects on marine
643 seismic attenuation measurements: Geophysical Prospecting, **47**, 1105-1119.

644 Hustoft, S., S. Bünz, J. Mienert, and S. Chand, 2009, Gas hydrate reservoir and active
645 methane-venting province in sediments on < 20 Ma young oceanic crust in the Fram Strait,
646 offshore NW-Svalbard: Earth and Planetary Science Letters, **284**, no. 1-2, 12-24.

647 Jacobson, R. S., G. G. Shor, Jr., and L. M. Dorman, 1981, Linear inversion of body
648 wave data- Part II: Attenuation versus depth using spectral ratios: Geophysics, **46**, 152-162.

649 Jaiswal, P., P. Dewangan, T. Ramprasad, and C. Zelt, 2012, Seismic characterization
650 of hydrates in faulted, fine-grained sediments of Krishna-Godavari Basin: full waveform
651 inversion: Journal of Geophysical Research, **117**, B10305, doi:10.1029/2012JB009201.

652 Jannsen, D., J. Voss, and F. Theilen, 1985, Comparison of methods to determine Q in
653 shallow marine sediments from vertical reflection seismograms: Geophysical Prospecting,
654 **33**, 479-497, doi: 10.1111/j.1365-2478.1985.tb00762.x.

655 Johnston, D. H., M. N. Toksöz, and A. Timur, 1979, Attenuation of seismic waves in
656 dry and saturated rocks: II. Mechanisms: Geophysics, **44,** 691-711.

657 Jung, J.-W., J. C. Santamarina, and K. Soga, 2012, Stress-strain response of hydrate-
658 bearing sands: Numerical study using discrete element method simulations: Journal of
659 Geophysical Research, **117**, B04202, doi: 10.1029/2011JB009040.

660 Korenaga, J., W. S. Holbrook, S. C. Singh, and T. A. Minshull, 1997, Natural gas
661 hydrates on the southeast US margins: Constraints from full waveform and traveltime
662 inversions of wide angle seismic data: Journal of Geophysical Research, **102**, 15345-15365.

663 Lee, M. W., and T. S. Collett, 2001, Elastic properties of gas hydrate-bearing
664 sediments: Geophysics, **66**, 763-771.

665 Lee, M. W., and T. S. Collett, 2006, Gas hydrate and free gas saturations estimated
666 form velocity logs on Hydrate ridge, offshore Oregon, USA, *in* A. M. Tréhu, G. Bohrmann,
667 M. E. Torres, and F. S. Colwell, eds., Proceedings of the Ocean Drilling Program, Scientific
668 Results, **204**: College Station TX (Ocean Drilling Program), 1-25.
669 doi:10.2973/odp.proc.sr.204.103.2006.

670 Liu, B., Q. Yuan, K. H. Su, X. Yang, B. C. Wu, C. Y. Sun, and G. J. Chen, 2012,
671 Experimental simulation of the exploitation of natural gas hydrate: Energies, **5**, 466-493, doi:
672 10.3390/en5020466.

673 Liu, X., and P. B. Flemings, 2007, Dynamic multiphase flow model of hydrate
674 formation in marine sediments: Journal of Geophysical Research, **112**, no. B3, B03101,
675 doi:10.1029/2005JB004227.

Matsushima, J., 2005, Attenuation measurements from sonic waveform logs in methane hydrate-bearing sediments at the Nankai Trough exploratory well off Tokai, central Japan: Geophysical Research Letters, **32**, L03306, 1-5, doi: 10.1029/2004GL021786.

Matsushima, J., 2006, Seismic wave attenuation in methane hydrate-bearing sediments: vertical seismic profiling data from the Nankai Trough exploratory well, offshore Tokai, central Japan: Journal of Geophysical Research, **111**, B10101, doi:10.1029/2005JB004031.

Mavko, G., T. Mukerji, and J. Dvorkin, 1998, The Rock Physics Handbook –Tools for Seismic Analysis in Porous Media: Cambridge University Press.

Mavko, G. M., and A. Nur, 1979, Wave attenuation in partially saturated rocks: Geophysics, **44**, 161–178.

Murphy, W. F., K. W. Winkler, and R. L. Kleinberg, 1986, Acoustic relaxation in sedimentary rocks: Dependence on grain contacts and fluid saturation: Geophysics, **51**, 757–766.

Ning, T., and L. Wen-kai, 2010, Improve Q estimates with spectrum correction based on seismic wavelet estimation: Applied Geophysics, **7**, 217-228, DOI: 10.1007/s11770-010-0252-2.

Nouzé, H., P. Henry, M. Noble, V. Martin, and G. Pascal, 2004, Large gas hydrate accumulations on the eastern Nankai Trough inferred from new high-resolution 2-D seismic data: Geophysical Research Letters, **31**, L13308, doi:10.1029/2004GL019848.

O'Connell, R. J., and B. Budiansky, 1977, Viscoelastic properties of fluid-saturated cracked solids: Journal of Geophysical Research, **82**, no. 36, 5719–5735.

O'Hara, S. G., 1989, Elastic-wave attenuation in fluid-saturated Berea sandstone: Geophysics, **54**, 785–788.

Parra, J. O., C. L. Hackert, and P.-C. Xu, 2002, Characterization of fractured low Q zones at the Buena Vista Hills reservoir, California: Geophysics, **67**, 1061–1070.

Petersen, C. J., S. Bünz, S. Hustoft, J. Mienert, and D. Klaeschen, 2010, High-resolution P-Cable 3D seismic imaging of gas chimney structures in gas hydrated sediments of an Arctic sediment drift: Marine and Petroleum Geology, **27**, no. 9, 1981-1994, doi: 10.1016/j.marpetgeo.2010.06.006.

Planke, S., F. N. Eriksen, C. Berndt, J. Mienert, and D. Masson, 2009, Spotlight on Technology: P-Cable High-Resolution Seismic: Oceanography, **22**, no. 1, 85.

Plaza-Faverola, A., S. Bünz, J. E. Johnson, S. Chand, J. Knies, J. Mienert, and P. Franek, 2015, Role of tectonic stress in seepage evolution along the gas hydrate charged Vestnesa Ridge, Fram Strait: Geophysical Research Letters, **42**, no. 3, 733-742, doi: 10.1002/2014GL062474.

Pointer, T., E. Liu, and J. A. Hudson, 2000, Seismic wave propagation in cracked porous media: Geophysical Journal International, **142**, 199–231.

Prasad, M., and A. Nur, 2003, Velocity and attenuation anisotropy in reservoir rocks: SEG, Expanded Abstracts, 1652-1655.

Pratt, R. G., K. Bauer, and M. Weber, 2003, Crosshole waveform tomography velocity and attenuation images of arctic gas hydrates: SEG, expanded abstracts, 2255-2258, doi: 10.1190/1.1817798.

719 Pratt, R. G, F. Hou, K. Bauer, and M. Weber, 2005, Waveform tomography images of
720 velocity and inelastic attenuation from the Mallik 2002 crosshole seismic surveys, *in* S. R.
721 Dallimore, and T. S. Collet, eds., Scientific results from the Mallik 2002 Gas Hydrate
722 Production Research Well Program, Mackenzie Delta, Northwest Territories, Canada:
723 Geological Survey of Canada, Bulletin 585, 1-14.

724 Priest, J. A., A. I. Best, and C. R. I. Clayton, 2006, Attenuation of seismic waves in
725 methane gas hydrate-bearing sand: Geophysical Journal International, **164**, 149-159, doi:
726 10.1111/j.1365-246X.2005.02831.x.

727 Quan, Y., and J. M. Harris, 1997, Seismic attenuation tomography using the
728 frequency shift method: Geophysics, **62**, 895-905.

729 Rapoport, M. B., L. I. Rapoport, and V. I. Ryjkov, 2004, Direct detection of oil and
730 gas fields based on seismic inelasticity effect: The Leading Edge, **23**, 276–278.

731 Reine, C., M. V. D. Baan, and R. Clark, 2009, The robustness of seismic attenuation
732 measurements using fixed- and variable-window time-frequency transforms: Geophysics, **74**,
733 no. 2, WA123-WA135, doi: 10.1190/1.3043726.

734 Riedel, M., T. S. Collett, P. Kumar, A. V. Sathe, and A. Cook, 2010, Seismic imaging
735 of a fractured gas hydrate system in the Krishna-Godavari basin offshore India: Marine and
736 Petroleum Geology, **27**, 1476-1493, doi: 10.1016/j.marpetgeo.2010.06.002.

737 Ritzmann, O., W. Jokat, W. Czuba, A. Guterch, R. Mjelde, and Y. Nishimura, 2004,
738 A deep seismic transect from Hovgård Ridge to northwestern Svalbard across the continental-
739 ocean transition: A sheared margin study: Geophysical Journal International, **157**, 683-702.

740 Rossi, G., D. Gei, G. Böhm, G. Madrussani, and J. M. Carcione, 2007, Attenuation
741 tomography: an application to gas-hydrate and free-gas detection: Geophysical Prospecting,
742 **55**, 655-669.

743 Ryu, B.-J., T. S. Collett, M. Riedel, G. Y. Kim, J. H. Chun, J. J. Bahk, J. Y. Lee, J. H.
744 Kim, and D. G. Yoo, 2013, Scientific results of the second gas hydrate drilling expedition in
745 the Ulleung basin (UBGH2): Marine and Petroleum Geology, **47**, 1-20, doi:
746 10.1016/j.marpetgeo.2013.07.007.

747 Sain, K., and A. K. Singh, 2011, Seismic quality factors across a bottom simulating
748 reflector in the Makran Accretionary Prism, Arabian Sea: Marine and Petroleum Geology,
749 **28**, no. 10, 1838-1843.

750 Sain, K., A. K. Singh, N. K. Thakur, and R. Khanna, 2009, Seismic quality factor
751 observations for gas-hydrate-bearing sediments on the western margin of India: Marine
752 Geophysical Researches, **30**, no. 3, 137-145, DOI: 10.1007/s11001-009-9073-1.

753 Sato, H., and M. C. Fehler, 1997, Seismic wave propagation and scattering in the
754 heterogeneous earth: Springer, doi:10.1007/978-3-540-89623-4.

755 Shipley T. H., M. H. Houston, R. T. Buffler, F. J. Shaub, K. J. McMillen, J. W. Ladd,
756 and J. L. Worzel, 1979, Seismic evidence for widespread possible gas hydrate horizons on
757 Continental slopes and Rises: The American Association of Petroleum Geologists Bulletin,
758 **63**, 2204-2213.

759 Sloan, E. D., 1998, Jr., Clathrate Hydrates of Natural Gases, 2nd edition: Marcel
760 Dekker Inc.

761 Smith, A. J., J. Mienert, S. Bünz, and J. Greinert, 2014, Thermogenic methane
762 injection via bubble transport into the upper Arctic Ocean from the hydrate ‐ charged
763 Vestnesa Ridge, Svalbard: Geochemistry, Geophysics, Geosystems, **15**, 1945–1959,
764 doi:10.1002/2013GC005179.

765 Spencer, J. W., Jr., 1979, Bulk and shear attenuation In Berea Sandstone: The effect
766 of pore fluids: Journal of Geophysical Research, **84**, 7521-7523.

767 Spencer, T. W., J. R. Sonnad, and T. M. Butler, 1982, Seismic Q — Stratigraphy or
768 dissipation: Geophysics, **47**, 16–24, doi: 10.1190/1.1441275.

769 Talukder, M. W., 2013, VSP P-wave attenuation model study in elastic earth: spectral
770 ratio method vs centroid frequency shift method: CSPG CSEG CWLS GeoConvention 2013,
771 Integration: Geoscience Engineering Partnership, Calgary, Canada.

772 Toksöz, M. N., and D. H. Johnston, 1981, Seismic wave attenuation: Geophysics
773 reprint series no. 2, Society of Exploration Geophysicists.

774 Toksöz, M. N., D. H. Johnston, and A. Timur, 1979, Attenuation of seismic waves in
775 dry and saturated rocks: I. Laboratory measurements: Geophysics, **44**, 681-690.

776 Tonn, R., 1991, The determination of the seismic quality factor Q from VSP data: A
777 comparison of different computational methods: Geophysical Prospecting, **39**, 1 – 27.

778 Vogt, P. R., K. Crane, E. Sundvor, M. D. Max, and S. L. Pfirman, 1994, Methane-
779 generated(?) pockmarks on young, thickly sedimented oceanic crust in the Arctic: Vestnesa
780 ridge, Fram strait: Geology, **22**, 255-258

781 Walsh, J. B., 1966, Seismic Wave Attenuation in Rock due to Friction: Journal of
782 Geophysical research, **71**, 2591-2599.

783 Wennerberg, L., 1993, Multiple-scattering Interpretations of coda-Q Measurements:
784 Bulletin of the Seismological Society of America, **83**, 279–290.

785 Winkler, K. W., and A. Nur, 1982, Seismic attenuation: Effects of pore fluids and
786 frictional-sliding: Geophysics, **47**, 1–15.

787 Winkler, K., A. Nur, and M. Gladwin, 1979, Friction and seismic attenuation in rocks:
788 Nature, **277**, 528–531.

789 Wood, W. T., W. S. Holbrook, and H. Hoskins, 2000, In situ measurements of P-wave
790 attenuation in methane hydrate and gas bearing sediments on the Blake Ridge, *in* C. K., Paull,
791 R. Matsumoto, P. J. Wallace, and W. P. Dillon, eds., Proceedings of the Ocean Drilling
792 Program, Scientific Results, **164**, 265-272.

793 Yoo, D. G., N. K. Kang, B. Y. Yi, G. Y. Kim, B. J. Ryu, K. Lee, G. H. Lee, and M.
794 Riedel, 2013, Occurrence and seismic characteristics of gas hydrate in the Ulleung basin, East
795 Sea offshore Korea: Marine and Petroleum Geology, **47**, 236-247,
796 doi:10.1016/j.marpetgeo.2013.07.001.

797 Zhang, H., S. Yang, N. Wu, X. Su, M. Holland, P. Schultheiss, K. Rose, H. Butler, G.
798 Humphrey, and GMS-1 Science Team, 2007, Successful and surprising results for China's
799 first gas hydrate drilling expedition: Fire in the Ice, **7**, no. 3, 6-9.

800

801 LIST OF FIGURES

802 Figure 1 Bathymetry map showing the location of our study area at Vestnesa Ridge,
803 on the west-Svalbard continental margin. The inset figure shows a seafloor time-structure
804 map derived from the 3D seismic data. Key inlines and crosslines are indicated on this
805 seafloor map. Two small boxes (B1 and B2) show the location of centroid frequency curves
806 plotted in Figure 5. A velocity model was derived from the multi-channel seismic (MCS) line
807 by Hustoft et al. (2009) (see also Figure 11d).

808 Figure 2 a) Amplitude spectrum of the seismic signal near the seafloor. b) Centroid
809 frequency of seismic signal in shallow sediments near the seafloor for different traces in
810 seismic data. The black line shows the assumed centroid frequency at the seafloor. c) The
811 blue curve shows the mean variance of the amplitude spectrum (σ_s^2) at different arrival times.
812 The red line shows the best fit line for changes of mean variance with two way travel time.

813 Figure 3 a) Sea floor reflection and BSR picked from a trace located at 26th inline and
814 260th crossline (see Figure 1 for location). b) Amplitude spectrum of the picked wavelets. c)
815 Plot of spectral ratio (in logarithmic scale) vs frequency. The red curve shows the best fit line
816 (L_1 norm) in this plot. Q is derived from the slope of the best fit line.

817 Figure 4 a) Selected seismic section (Inline 115, see Figure 1 for location) from the
818 3D seismic data. b) Centroid frequency plot corresponding to the seismic section. Black
819 arrows indicate the possible sub-surface fluid migration through gas chimneys and
820 subsequent seafloor gas seepage. c) Acoustic flares documenting active seepage (modified
821 from Bünz et al., 2012). The black line shows the location of the inline shown in a) and b).

822 Figure 5 a) Seismic trace corresponding to 183rd Inline and 1093rd crossline (location
823 of the trace lies in the center of B1 as shown in Figure 1). Q has been estimated for the L1,

L2, L3, L4 and L5 intervals. b) Centroid frequencies calculated in the 5 ms sliding time window (Figure 5a). c) Centroid frequency trend/curve for 25 traces in a 31.25 x 31.25 m^2 small box B1 (Figure 1). d) The black curve shows the centroid frequency curve. The green curves show the synthetic centroid frequency curves corresponding to Q model 1 (Q_{L1}=500 , Q_{L2}=400, Q_{L3}=300, Q_{L4}=200, and Q_{L5}=100), Q model 2 (Q_{L1}=70, Q_{L2}=100, Q_{L3}=200, Q_{L4}=300, and Q_{L5}=500), Q model 3 (Q_{L1}=150, Q_{L2}=125, Q_{L3}=100, Q_{L4}=75, and Q_{L5}=50), Q model 4 (Q_{L1}=50, Q_{L2}=75, Q_{L3}=150, Q_{L4}=30, and Q_{L5}=200), and Q model 5 (Q_{L1}=90, Q_{L2}=65, Q_{L3}=50, Q_{L4}=40, and Q_{L5}=30). The red curve shows the synthetic centroid frequency curve for the best fit (L_1 norm) Q model. b) 5 layer best fit Q model (red) and 7 layer best fit Q model (green) for a centroid frequency curve (location shown by a small box B2 in Figure 1).

Figure 6 a) Seismic section of Inline 69 (see Figure 1 for location) with picked seafloor and three major subsurface reflections. L1, L2, L3, and L4 show the layers for which Q is estimated. b) Overlay of seismic section and Q estimates obtained from centroid frequency shift method. c) Overlay of seismic section and Q estimates obtained from spectral ratio method.

Figure 7 Q slices for different layers estimated using centroid frequency shift method. Q slices (a), (b), (c), and (d) correspond to layers L1, L2, L3, and L4 (Figure 6a) respectively.

Figure 8 a) Seismic trace corresponding to 98^{th} inline and 686^{th} crossline (see Figure 1 for location). L1, L2, L3, and L4 are four layers between five reflections (R_1, R_2, R_3, R_4, and R_5). b) AS_1, AS_2, AS_3, AS_4, and AS_5 are amplitude spectra calculated over time windows R_1, R_2, R_3, R_4, and R_5 respectively. c), d), e), and f) show spectral ratio vs frequency plot. The red lines show the best fit line derived using L_1 norm. Q_{L1}, Q_{L2}, Q_{L3}, and Q_{L4} are the derived Q values for layers L1, L2, L3, and L4 respectively.

Figure 9 Q slices for different layers estimated using spectral ratio method. Q slices (a), (b), (c), and (d) correspond to layers L1, L2, L3, and L4 (Figure 6a) respectively.

Figure 10 a) Histogram of Q values obtained using centroid frequency shift method in the layer L3. b) Histogram of Q values obtained using centroid frequency shift method in the layer L3 with Q<30 (high concentration of free gas) in the layer L4. c) Ratio of histogram b and histogram a. d) Histogram of Q values obtained using spectral ratio method in the layer L3. e) Histogram of Q values obtained using spectral ratio method in the layer L3 with Q<30 (high concentration of free gas) in the layer L4. f) Ratio of histogram e and histogram d. Layers L1, L2, L3 and L4 are shown in Figure 6a.

Figure 11 a) Variance map obtained from a time slice at BSR depth showing several faults (Plaza-Faverola et al., 2015) and gas chimneys (Bünz et al., 2012) piercing through the subsurface. b) Q slice obtained by overlaying (through 50% transparency) Q slices from spectral ratio method (Figure 9c) and centroid frequency shift method (Figure 7c) in the layer L3 (layer above the BSR). c) Q slice obtained by overlaying (through 50% transparency) Q slices from spectral ratio method (Figure 9d) and centroid frequency shift method (Figure 7d) in the layer L4 (layer below the BSR). d) P-wave velocity cross-section derived using multi-channel seismic profile (see Figure 1 for location) across Vestnesa Ridge (modified from Hustoft et al., 2009). Arrows in the Figure show upslope gas migration and its leakage from the Vestnesa Ridge.

Figure 1

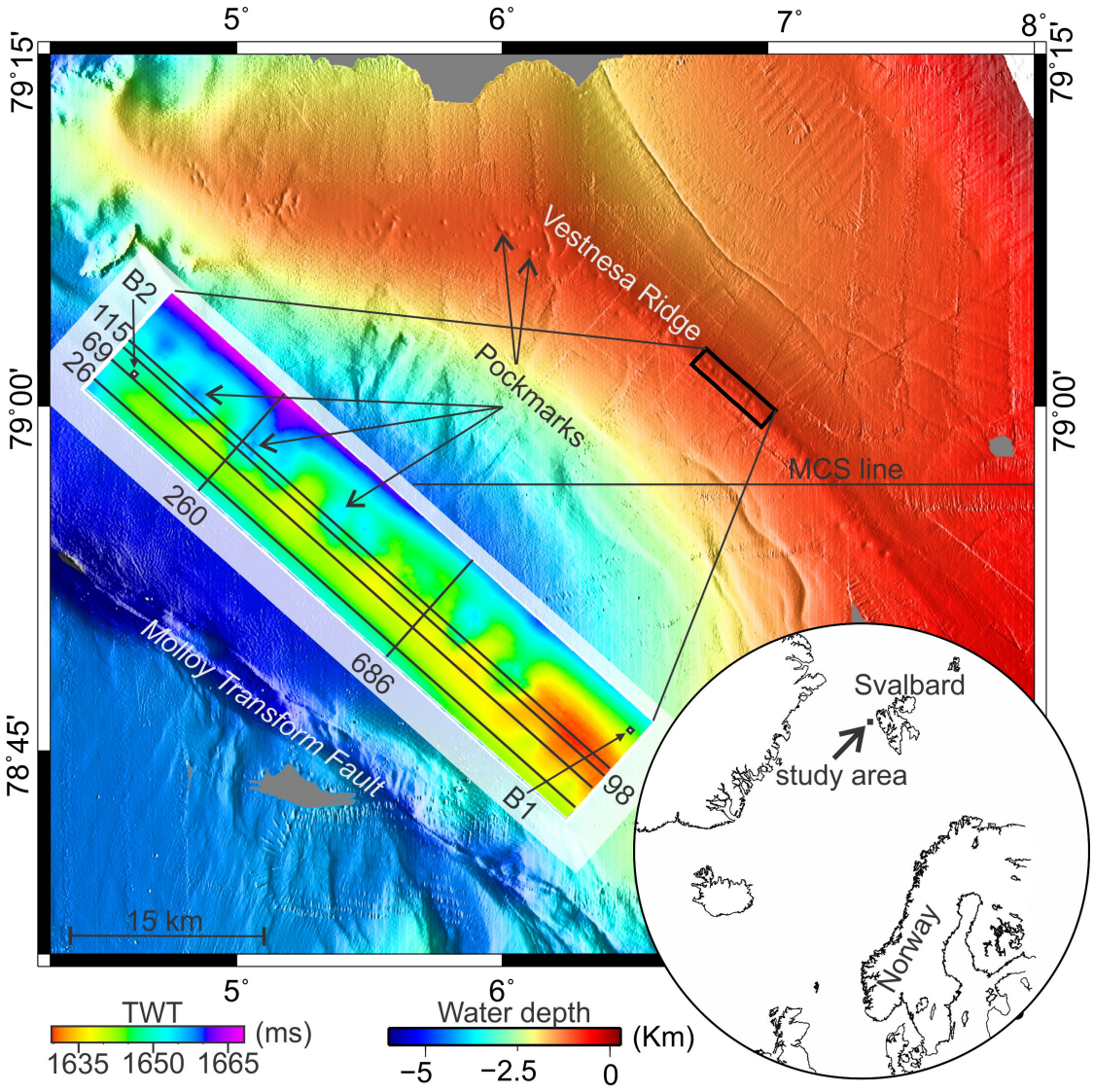
5˚
6˚
7˚
8˚
79˚15'
79˚00'
78˚45'
Vestnesa Ridge
Pockmarks
MCS line
B2
115
69
26
260
686
98
B1
Molloy Transform Fault
15 km
Svalbard
study area
Norway
TWT
(ms)
1635 1650 1665
Water depth
(Km)
−5 −2.5 0

Figure 2

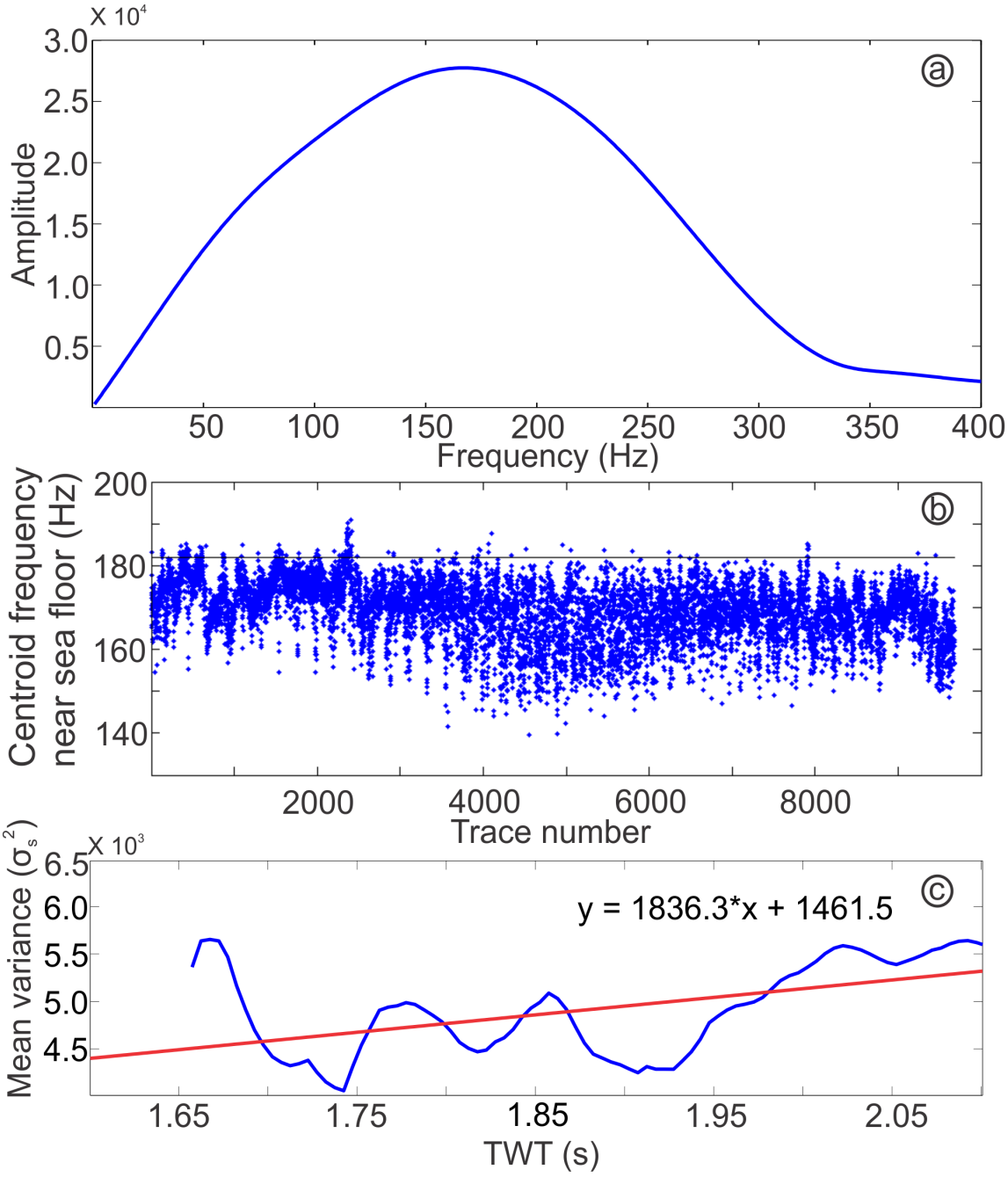
X 10^4
3.0
2.5
2.0
1.5
1.0
0.5
Amplitude
ⓐ
50
100
150
200
250
300
350
400
Frequency (Hz)
Centroid frequency near sea floor (Hz)
200
180
160
140
ⓑ
2000
4000
6000
8000
Trace number
Mean variance (σs^2)
X 10^3
6.5
6.0
5.5
5.0
4.5
y = 1836.3*x + 1461.5
ⓒ
1.65
1.75
1.85
1.95
2.05
TWT (s)

Figure 3

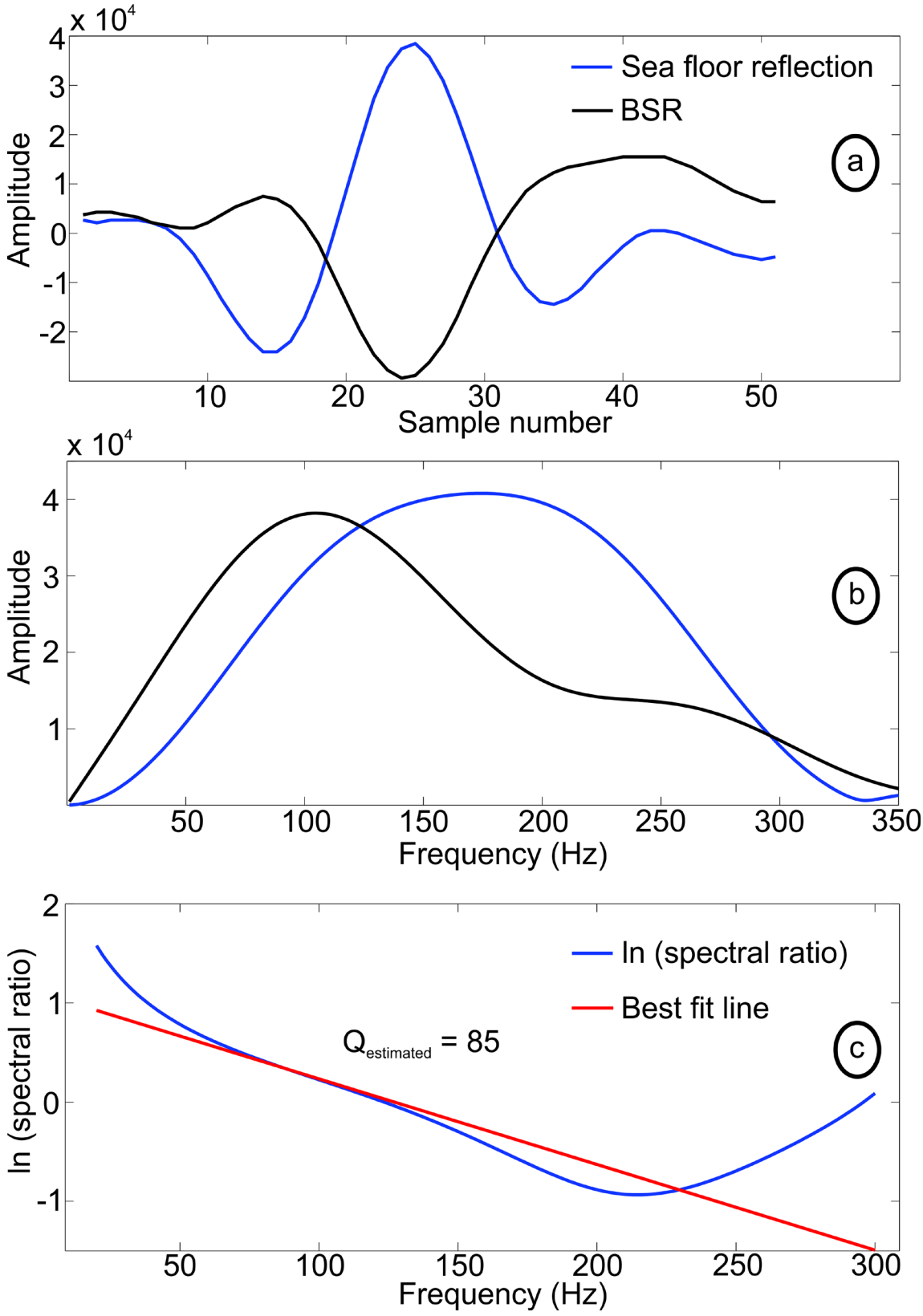
x 10^4
Amplitude
Sea floor reflection
BSR
a
Sample number
x 10^4
Amplitude
b
Frequency (Hz)
ln (spectral ratio)
Best fit line
Q_estimated = 85
c
Frequency (Hz)

Figure 4

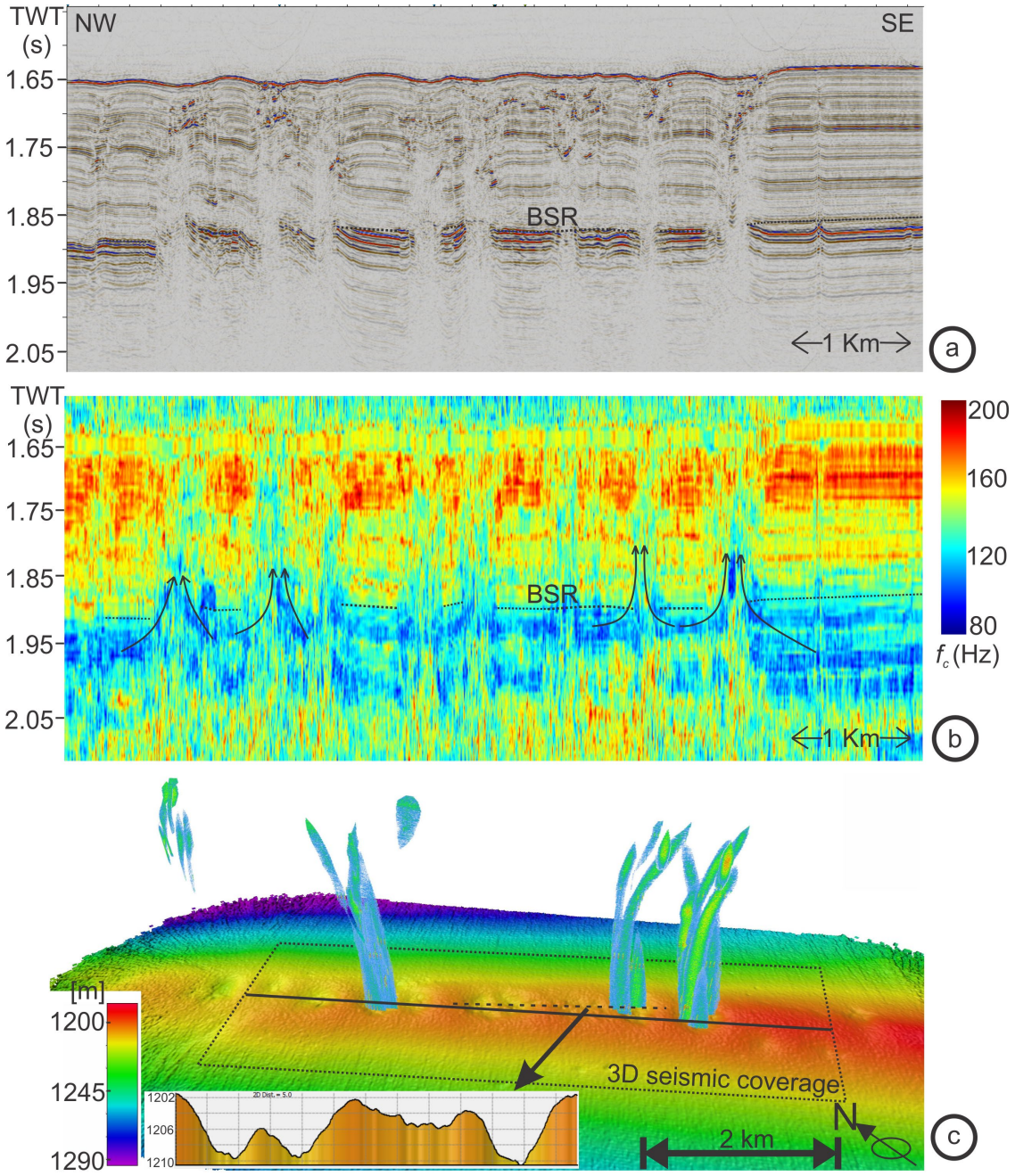
TWT (s)
NW
SE
1.65
1.75
1.85
1.95
2.05
BSR
←1 Km→
a
TWT (s)
1.65
1.75
1.85
1.95
2.05
BSR
←1 Km→
b
200
160
120
80
f_c (Hz)
[m]
1200
1245
1290
1202
1206
1210
3D seismic coverage
N
2 km
c

Figure 5

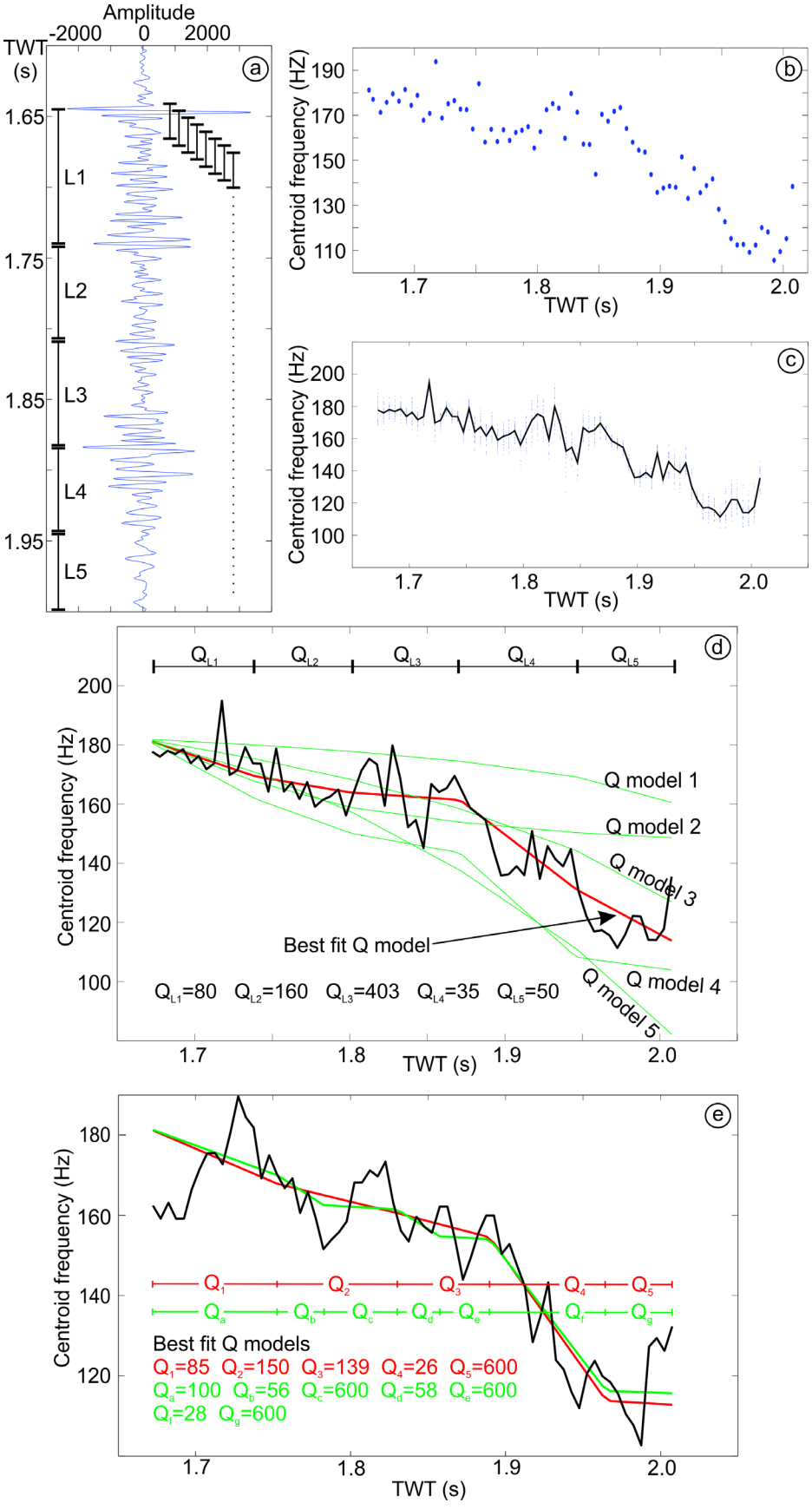
Amplitude
-2000
0
2000
TWT (s)
1.65
1.75
1.85
1.95
L1
L2
L3
L4
L5
a
Centroid frequency (HZ)
190
170
150
130
110
1.7
1.8
1.9
2.0
TWT (s)
b
Centroid frequency (Hz)
200
180
160
140
120
100
c
d
Q_{L1} Q_{L2} Q_{L3} Q_{L4} Q_{L5}
Q model 1
Q model 2
Q model 3
Q model 4
Q model 5
Best fit Q model
Q_{L1}=80 Q_{L2}=160 Q_{L3}=403 Q_{L4}=35 Q_{L5}=50
e
Q_1 Q_2 Q_3 Q_4 Q_5
Q_a Q_b Q_c Q_d Q_e Q_f Q_g
Best fit Q models
Q_1=85 Q_2=150 Q_3=139 Q_4=26 Q_5=600
Q_a=100 Q_b=56 Q_c=600 Q_d=58 Q_e=600
Q_f=28 Q_g=600

Figure 6

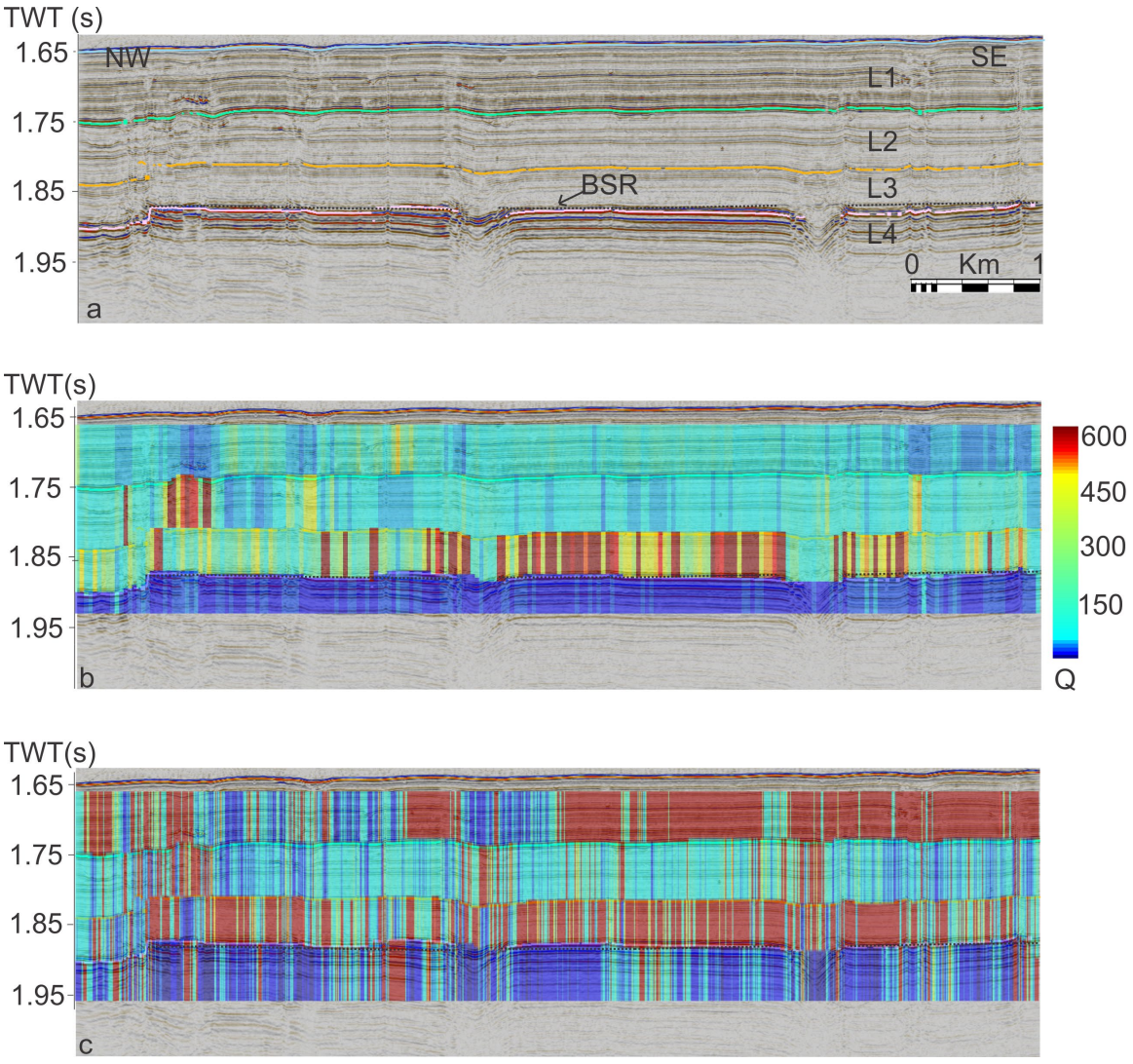
TWT (s)
1.65
1.75
1.85
1.95
NW
SE
L1
L2
L3
L4
BSR
0 Km 1
a
TWT(s)
1.65
1.75
1.85
1.95
b
600
450
300
150
Q
TWT(s)
1.65
1.75
1.85
1.95
c

Figure 7

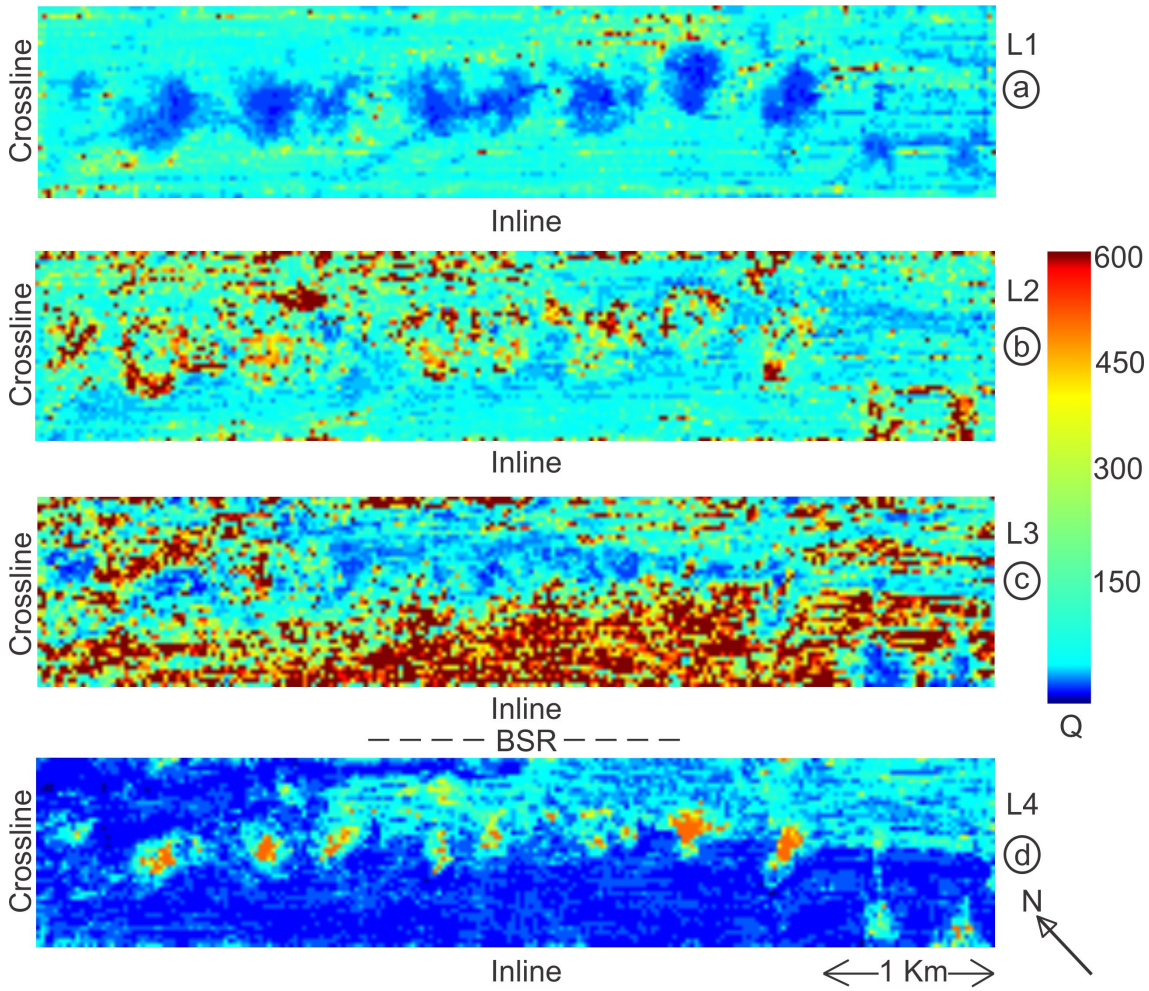

Figure 8

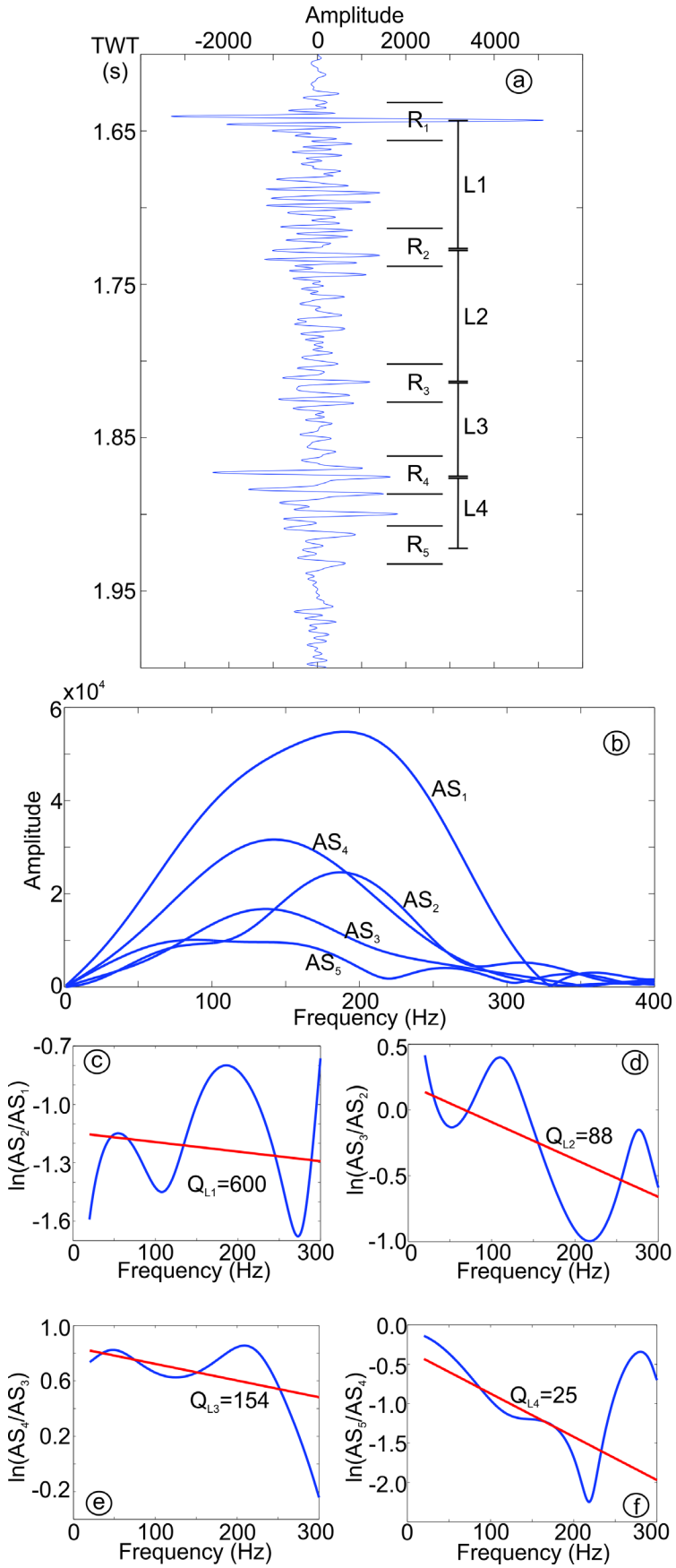
Amplitude
TWT (s)
-2000
0
2000
4000
1.65
1.75
1.85
1.95
R1
R2
R3
R4
R5
L1
L2
L3
L4
a
x10^4
Amplitude
Frequency (Hz)
AS1
AS4
AS2
AS3
AS5
b
ln(AS2/AS1)
QL1=600
c
ln(AS3/AS2)
QL2=88
d
ln(AS4/AS3)
QL3=154
e
ln(AS5/AS4)
QL4=25
f

Figure 9

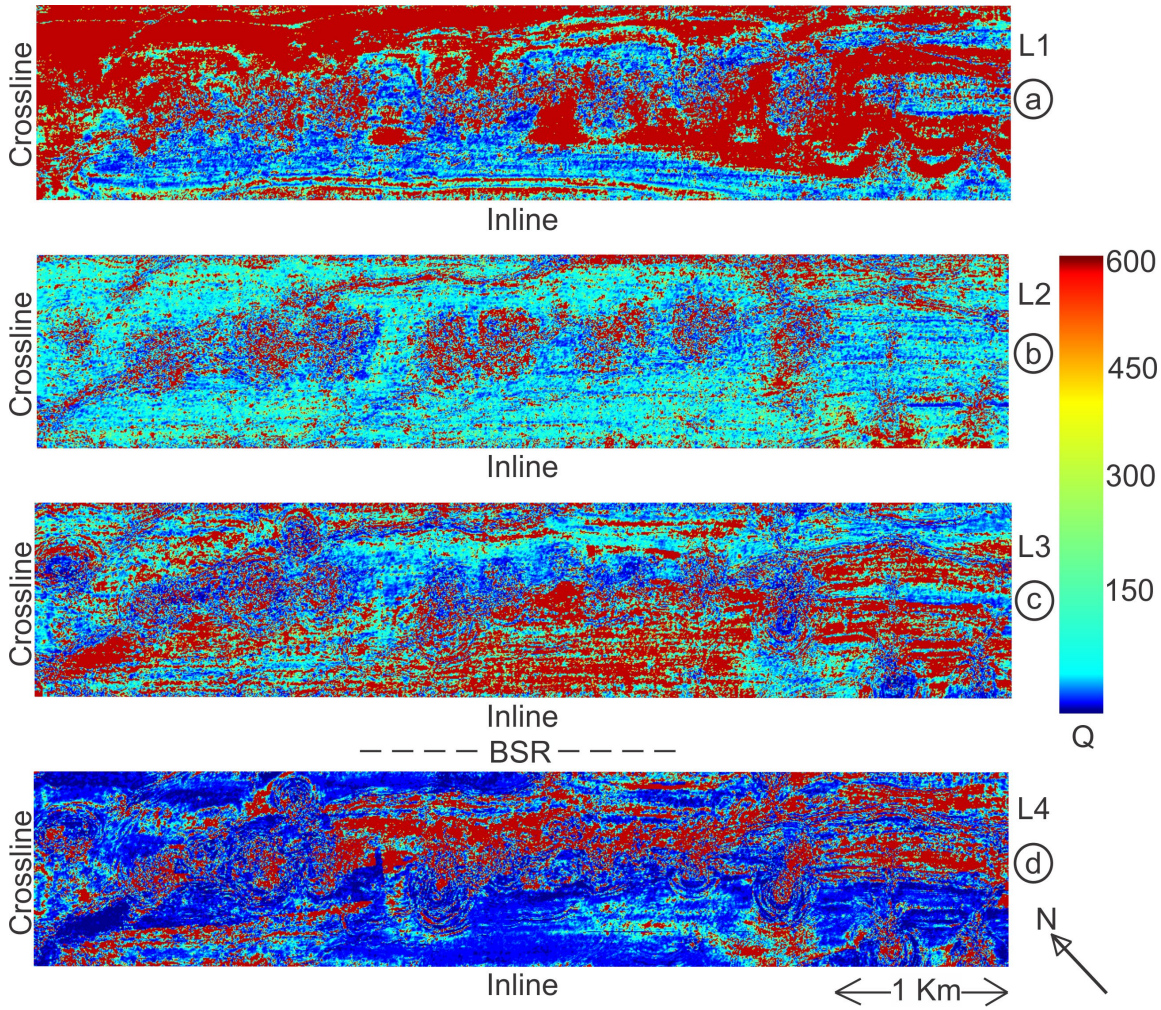

Figure 10

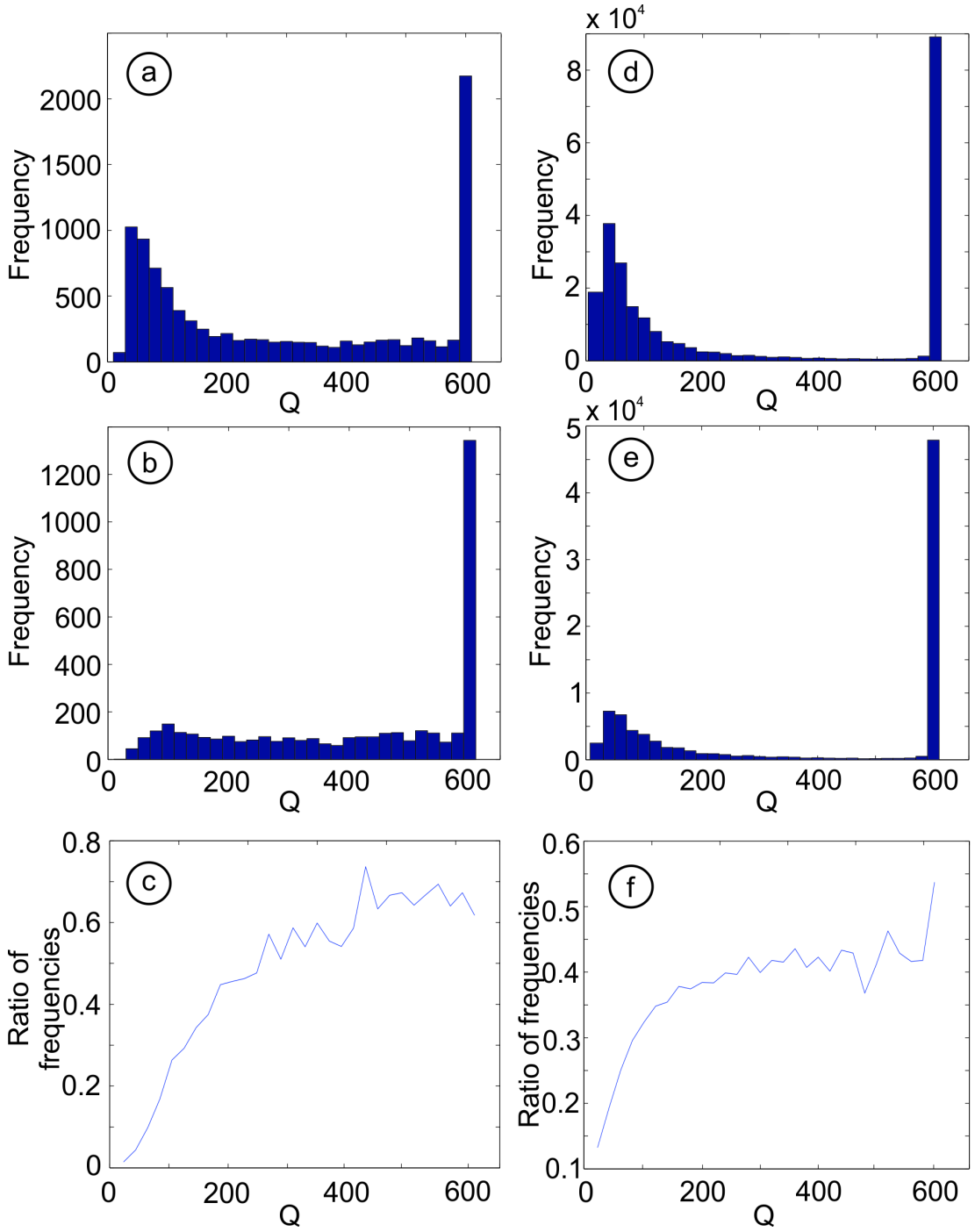
a
b
c
d
e
f
Frequency
Ratio of frequencies
Q
x 10^4
0
200
400
600
500
1000
1500
2000
800
1200
2
4
6
8
1
3
5
0.1
0.2
0.3
0.4
0.5
0.6
0.8

Figure 11

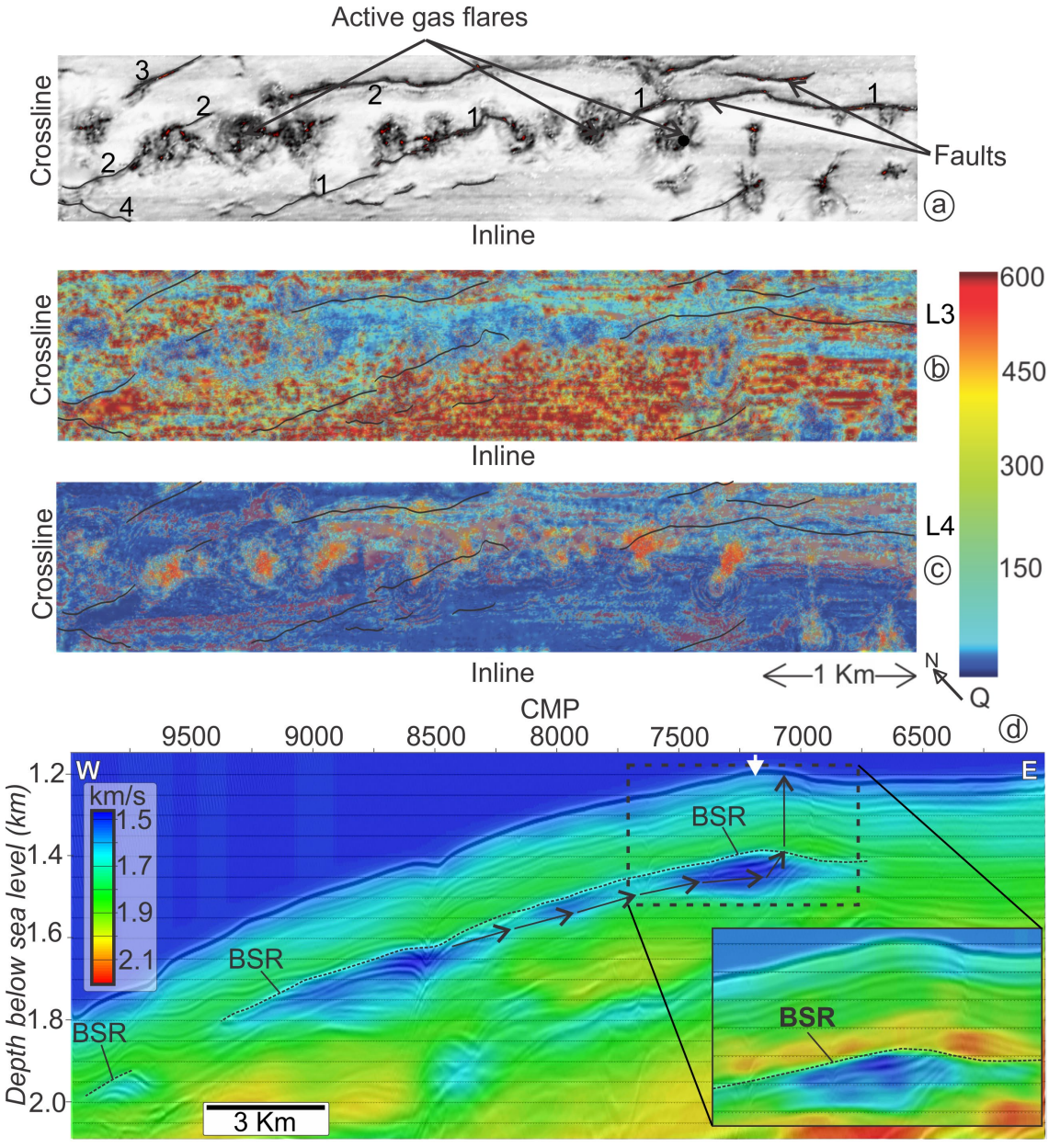
Active gas flares
Crossline
Inline
Faults
a
b
c
d
L3
L4
600
450
300
150
1 Km
N
Q
CMP
9500
9000
8500
8000
7500
7000
6500
W
E
km/s
1.5
1.7
1.9
2.1
BSR
3 Km
Depth below sea level (km)
1.2
1.4
1.6
1.8
2.0